January, 2010

ASACUSA STATUS REPORT

ASACUSA progress during 2009 and plans for 2010

CERN-SPSC-2010-005 / SPSC-SR-056
20/01/2010

ASACUSA collaboration

D. Barna[1,6], M. Charlton[2], M. Corradini[3], A. Dax[1], Y. Enomoto[5], S. Federmann[8], S. Friedreich[8], R.S. Hayano[1], H. Higaki[5], M. Hori[1,11], D. Horváth[6], C.A. Hunniford[9], B. Juhász[8], Y. Kanai[5], C. Kim[4], H. Knudsen[7], H-P. Kristiansen[7], T. Kobayashi[1], N. Kuroda[4], M. Leali[3], E. Lodi-Rizzini[3], M. Lund[7], V. Mascagna[3], O. Massiczek[8], Y. Matsuda[4], R.W. McCullough[9], K. Michishio[5], S.P. Møller[7], T. Pask[8], W. Pirkl[1], A. Sótér[11], K. Todoroki[1], K. Tőkési[10], H.D. Thomsen[7], H.A. Torii[4], U. Uggerhøj[7], L. Venturelli[3], E. Widmann[8], Y. Yamazaki[5], P. Zalán[6], J. Zmeskal[8], N. Zurlo[3]

1. The University of Tokyo (JP), 2. University of Swansea (GB), 3. Università di Brescia and INFN (IT), 4. The University of Tokyo, Komaba (JP), 5. RIKEN (JP), 6. KFKI (HU), 7. University of Aarhus (DK), 8. Stefan Meyer Institute (AT), 9. The Queen's University of Belfast (UK), 10. ATOMKI (HU), 11 Max-Planck-Institut für Quantenoptik (DE)

Executive Summary

Antiprotonic Helium Laser Spectroscopy ($\bar{p}$ mass)

1. We measured four transitions in $\overline{p}^3\mathrm{He}^+$ which had in previous experiments showed a 2σ difference compared to the results ν_{th} of three-body QED calculations. The newly-obtained ν_{exp} values were within 10–15 parts per billion of ν_{th}. These measurements must be extended in 2010 to all 12 transitions of both $\overline{p}^4\mathrm{He}^+$ and $\overline{p}^3\mathrm{He}^+$ if we are to derive a new value for the electron-to-antiproton mass ratio.
2. We systematically measured the Auger rates γ_A of six $\overline{p}\mathrm{He}^+$ states (of which four states appeared to have decay rates between 3 and 100 times larger than the theoretical ones in our previous measurement). All measured Auger rates γ_A now agree with theoretical calculations within the experimental errors of $10-25\%$.

Antiprotonic Helium Microwave Spectroscopy ($\bar{p}$ magnetic moment)

4. The results on the hyperfine structure of the $(37,35)$ state of $\overline{\mathrm{p}}^4\mathrm{He}$ was published, in which a new experimental value of the spin magnetic moment of the antiproton was obtained as $\mu_s^{\overline{\mathrm{p}}} = -2.7862(83)\mu_N$, improving the previously best measurement.
5. The measurement of a new state has been started: the (n,L) = (36, 34) state of $\overline{\mathrm{p}}^3\mathrm{He}^+$. A comparison between the theoretical calculations and experimental results would lead to a more rigorous test of the theory and address any systematic errors therein.

Antihydrogen Ground-state Hyperfine Splitting

7. Using the "CUSP" trap, we achieved in 2009 (1) more than ten times higher accumulation rate of positrons than in 2008, (2) positron compression in the non-uniform cusp magnetic field, (3) stable mixing of antiprotons and positrons followed by cooling of antiprotons in the non-uniform cusp magnetic field, (4) non-destructive monitoring of the number of antiprotons, etc. In order to confirm the formation of $\bar{\mathrm{H}}$ atoms, we need in 2010 to further improve the trap vacuum and to lower the positron temperature.
8. During 2009, the work towards building the radio-frequency resonator for the ground-state antihydrogen hyperfine splitting measurement was started at CERN with the help of the BE-RF group.
9. Another important component of the atomic beam apparatus, the superconducting sextupole magnet, was ordered in 2009 through CERN from Tesla Engineering in the UK, following a market survey and a tendering process at CERN.

Atomic and nuclear collision experiments

10. Our $\bar{p}$-hydrogen ionization cross section measurement in 2009 was hampered by problems with the availability of ultra slow antiproton beam. We did, however, measure a few data points for the ionization of molecular hydrogen. At 10 keV, the new data confirm the magnitude of our measurements obtained at LEAR, where a very different experimental method was employed.
11. In 2009 the second phase of the measurement of the antiproton annihilation cross section (σ_{ann}) was started. The present data indicate that the main sources of background are under control and with an increase of the quality of the antiproton beam on the target the 100 keV measurement is feasible.

Beam usage plan for 2010

"CUSP" trap - antihydrogen beam extraction from the trap	9.5 weeks
Antiproton-hydrogen ionization cross section measurement	2 weeks
Antiprotonic helium-3 microwave resonance	4 weeks
Antiproton-nucleus annihilation cross section at 100 keV	2 weeks
Antiprotonic helium laser spectroscopy	9.5 weeks
Total = 28 AD weeks - AD4	27 weeks

Contents

1 Antiprotonic Helium Laser Spectroscopy **1**
- 1.1 Improvements in precision laser spectroscopy of antiprotonic helium . . . 1
- 1.2 Doppler-free saturation spectroscopy of antiprotonic helium . . . 4
- 1.3 Precise measurements of the lifetimes of $\overline{p}\mathrm{He}^+$ states . . . 5
- 1.4 Plans for 2010 - Spectroscopy of very cold $\overline{p}\mathrm{He}^+$ atoms . . . 5

2 Spectroscopy of the Hyperfine Structure of Antiprotonic Helium **6**
- 2.1 Introduction . . . 6
- 2.2 Hyperfine Structure . . . 8
- 2.3 Experimental Method . . . 10
- 2.4 Experimental Apparatus . . . 11
- 2.5 2009 Measurements . . . 11
- 2.6 Proposed Measurements in 2010 and Beamtime Request . . . 12

3 Cusp trap experiment for $\bar{H}$ synthesis and ground-state hyperfine spectroscopy **13**
- 3.1 Status of the MUSASHI $\bar{p}$ accumulator . . . 13
- 3.2 Positron pre-accumulator . . . 16
- 3.3 Mixing $\bar{p}$ and e^+ in the Cusp trap . . . 18
- 3.4 3D detector for the cusp trap . . . 22
- 3.5 Antihydrogen sextupole beamline . . . 24
- 3.6 Summary of 2009 and plan for 2010 . . . 25

4 Ionization of atoms and molecules by slow antiprotons **28**

5 Antiproton-nuclei cross sections experiment at 100 keV **29**
- 5.1 2009 Measurements . . . 29
- 5.2 Plans for 2010 . . . 32

6 Development of a superconducting radiofrequency Paul trap for antiprotons **32**

1 Antiprotonic Helium Laser Spectroscopy

1.1 Improvements in precision laser spectroscopy of antiprotonic helium

In 2009, we utilized new laser systems [1] and an improved experimental target to measure four transition frequencies in $\overline{p}^3\mathrm{He}^+$, which had in previous experiments [2] showed a 2-σ difference compared to the results ν_{th} of three-body QED calculations [3]. After using various experimental techniques to eliminate some higher-order systematic effects associated with the thermal Doppler motion [4] of the $\overline{p}^3\mathrm{He}^+$ in the target (see below), we found that the newly measured frequencies ν_{exp} are all within 10–15 parts per billion of ν_{th}. These measurements will be continued in 2010.

The Committee on Data for Science and Technology (CODATA) has recently described [5] the 2006 self-consistent set of values of the basic constants and conversion factors of physics and chemistry for international use. Twelve transition frequencies ν_{exp} in the $\overline{p}^4\mathrm{He}^+$ and $\overline{p}^3\mathrm{He}^+$ isotopes measured by ASACUSA's laser spectroscopy experiments [2,6–9] to a fractional precision of $\sim 10^{-8}$ were included as part of this data set to determine the electron-to-(anti)proton mass ratio (m_e/m_p). The derivation of $m_e/m_{\overline{p}}$ was carried out by comparing ν_{exp} with ν_{th} [3]. This result, when combined with the cyclotron frequency of the antiproton measured by the ATRAP experiment [10] to a much higher precision of 9 parts in 10^{11} also indicate that any CPT-violating difference between the antiproton mass and charge, and those of the proton must be less than 2 parts in 10^9 [11].

Fig. 1 shows the deviations of the experimental (circles with 1σ errors) and calculated frequencies $(\nu_{\mathrm{th}}-\nu_{\mathrm{exp}})/\nu_{\mathrm{exp}}$ published in 2006. For the four highest-precision measurements in $\overline{p}^4\mathrm{He}^+$ and $(n,\ell)=(36,34)\rightarrow(37,33)$ in $\overline{p}^3\mathrm{He}^+$ the agreement was better than 10 parts per billion. Four of experimental $\overline{p}^3\mathrm{He}^+$ frequencies, however, were $\sim 2\sigma$ below the calculated ones. CODATA has noted [5] that,

The separate inferred values [of the electron mass $A_r(e)$] *from the* $\overline{p}^4He^+$ *and* $\overline{p}^3He^+$ *frequencies differ somewhat, but the values from all 12 frequencies not only agrees with the three other available results for*

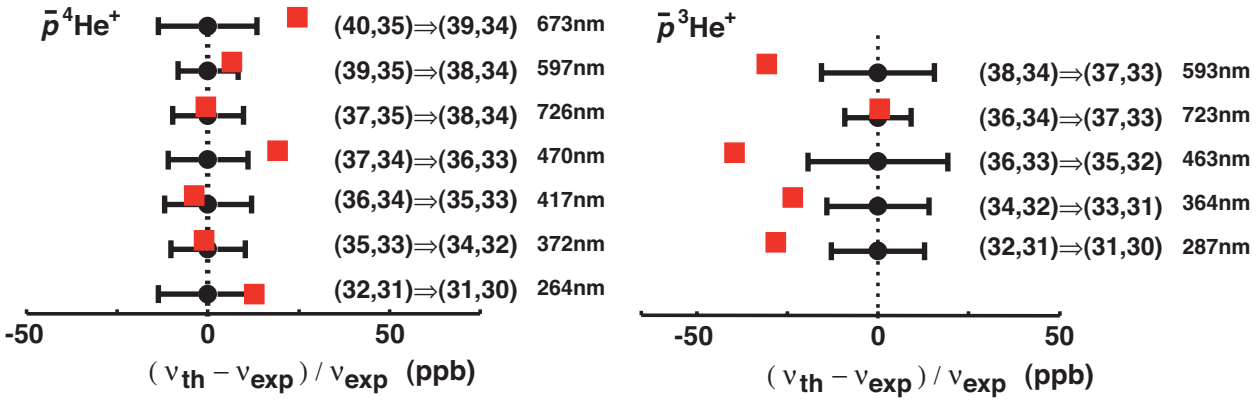

Figure 1: *Experimental* ν_{exp} *(circles with* 1σ *errors) [2] vs theoretical* ν_{th} *[3] transition frequencies used in 2006 to determine the antiproton-to-electron mass ratio. For the four highest-precision measurements in* $\overline{p}^4\mathrm{He}^+$*, and* $(n,\ell)=(36,34)\rightarrow(37,33)$ *in* $\overline{p}^3\mathrm{He}^+$ *the agreement was better than 10 parts per billion. Four of experimental* $\overline{p}^3\mathrm{He}^+$ *frequencies, however, were* $\sim 2\sigma$ *below the calculated ones.*

$A_r(e)$, but has a competitive level of uncertainty as well.

To further improve the precision on $m_e/m_{\overline{p}}$, it is vital to study the possible reasons for the 2-σ difference between $\nu_{\rm exp}$ and $\nu_{\rm th}$ in the four $\overline{p}^3{\rm He}^+$ transitions of Fig. 1. Our recent sub-Doppler saturation spectroscopy experiments and theoretical studies [4] revealed a new possible source of systematic shift in $\nu_{\rm exp}$. In Ref. [2], antiprotons of energy ~ 100 keV were allowed to enter a 150-mm-diameter, 300-mm-long stainless steel chamber filled with helium gas of temperature $T \sim 10$ K (see Fig. 2 (a)). The antiprotons slowed down and stopped in the helium gas, thereby producing $\overline{p}{\rm He}^+$ atoms. A pulsed laser beam entered the chamber through a fused silica window fixed on the opposite end of the chamber, anti-collinear with the antiproton beam. This geometry caused part of the laser beam to reflect or scatter off the stainless steel walls and flanges of the target, so that the $\overline{p}{\rm He}^+$ atoms were simultaneously irradiated by laser light from several directions.

This can cause deformations in the observed resonance lines of $\overline{p}{\rm He}^+$. First, the lines are broadened by the thermal Doppler motion of the atoms in the target to a value equivalent to,

$$\Delta\nu = 2.35\nu\sqrt{\frac{kT}{Mc^2}}, \tag{1}$$

wherein M and T denote the mass and temperature of the atom, k the Boltzmann constant, and c the speed of light. This broadening would normally be symmetric with respect to $\nu_{\rm exp}$ if the atoms were irradiated by a single collimated laser beam. However, since in the actual experiments the atoms were irradiated by multiple beams reflecting and scattering in the target, different parts of the atom's thermal distribution were depopulated simultaneously. Under certain conditions, the resonance profile can then become skewed, so that the value of $\nu_{\rm exp}$ derived from the spectra are systematically shifted. This effect appears stronger in $\overline{p}^3{\rm He}^+$ due to its complicated hyperfine structure consisting of eight sublines [4] arising from the spin interactions between the three constituent particles[1]. The spacings between these sublines are highly asymmetric. By comparison, $\overline{p}^4{\rm He}^+$ has four hyperfine sublines which are relatively symmetrically spaced[2].

To solve this problem we used the setup shown in Fig. 2 (b), wherein the antiproton and laser beams were allowed to intersect at a 90-degree angle. Antiprotons of energy 5.3 MeV extracted from the AD were decelerated to energy 80 keV using the radiofrequency quadrupole decelerator (RFQD), and entered the target through a 1.2-μm-thick plastic window. The laser beam entered through a quartz window fixed on the left side of the target at Brewster's angle, and exited though another window on the right. In this way the above problems of scattered or reflected light were avoided, and the $\overline{p}{\rm He}^+$ were irradiated by a single collimated laser beam of diameter ~ 20 mm.

We also constructed three lasers with spectral linewidths ~ 10 times narrower than those used in Ref. [2]. One of these was a pulsed Nd:YAG ring laser of wavelength $\lambda = 1064$ nm which was pumped by an array of semiconductor diode lasers of 808 nm. It produced 100-ns-long laser pulses of energy 600 mJ in a single longitudinal mode. This beam was frequency-doubled to wavelength $\lambda = 532$ nm using a BBO nonlinear crystal, and used to pump a cw pulse-amplified dye laser. We constructed two pulsed Ti:Sapphire lasers whose optical frequencies were stabilized with a precision of better than 1 part in 10^9 [1]. Each laser produced 30–60-ns-long laser pulses of energy 80 mJ and wavelength $\lambda = 792$–888 nm. These beams were frequency tripled in a series of LBO and BBO crystals to generate the UV laser pulses of $\lambda = 264$ and 296 nm. The frequencies of the Ti:Sapphire lasers were stabilized against an optical frequency comb generator [12,13], itself referenced to a 10-MHz quartz oscillator disciplined by a global positioning satellite

[1]Fig. 8 shows the octuplet structure of a state (n,L) of $\bar{p}^3{\rm He}^+$. Laser-induced transitions between (n,L) and $(n\pm1,L-1)$ then exhibit eight sublines.

[2]Fig. 7 shows the quadruplet structure of a state (n,L) of $\bar{p}^4{\rm He}^+$. Laser-induced transitions between (n,L) and $(n\pm1,L-1)$ then exhibit four sublines.

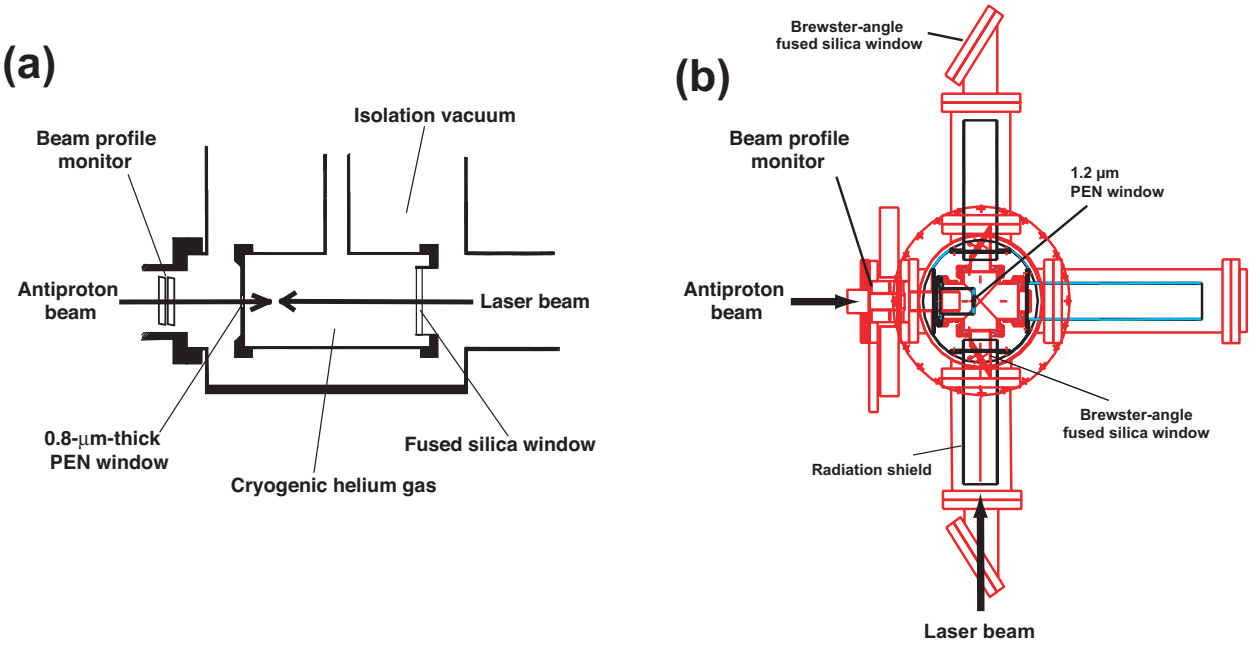

Figure 2: *Setup of laser spectroscopy experiment in 2006 [2], compared to that of 2009. The laser and antiproton beams were previously anti-collinear, but in 2009 it was changed to a 90-degree arrangement. This avoids the background signal due to laser light scattered on the windows and chamber walls.*

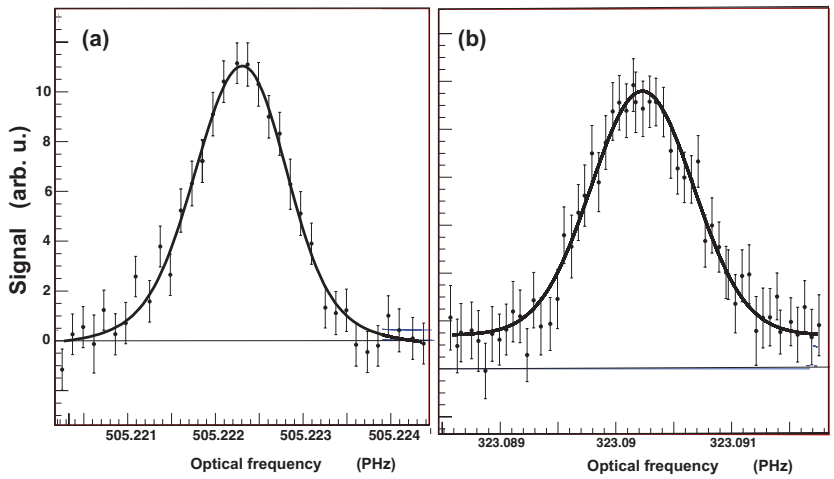

Figure 3: *Spectra of the* $(n,\ell) = (38,34) \rightarrow (37,33)$ *transition of wavelength* $\lambda = 593.4$ *nm (a) and* $(36,33) \rightarrow (35,32)$ *of 463.9 nm (b) of* $\bar{p}^3He^+$ *measured in 2009 using the new target and laser systems. Note small statistical fluctuation.*

(GPS) receiver. The linewidth ($\sim$ 6 MHz) of this laser was among the narrowest for any nanosecond laser with megawatt-scale output powers [1].

Fig. 3 shows typical spectra of the $(n,\ell) = (38,34) \rightarrow (37,33)$ transition of wavelength $\lambda = 593.4$ nm and $(36,33) \rightarrow (35,32)$ of 463.9 nm measured using the new target and laser systems. Due to the high spectral purity of the lasers, the resonances are characterized by high signal-to-noise ratios and small statistical

fluctuation. The linewidths $\Gamma \sim 1$ GHz of these lines contain contributions from the thermal Doppler width, the hyperfine structure, and the natural width of the daughter states $(37,33)$ and $(35,32)$. We measured two other transitions $(34,32)\rightarrow(33,31)$ of 364.7 nm and $(32,31)\rightarrow(31,30)$ of 287.8 nm. The experimental precision of the four transitions was around 9–13 parts per billion, whereas $\nu_{\rm exp}$ and $\nu_{\rm th}$ agreed within the 1-σ experimental errors. We will continue these measurements in 2010 to study other transitions with even higher precision.

1.2 Doppler-free saturation spectroscopy of antiprotonic helium

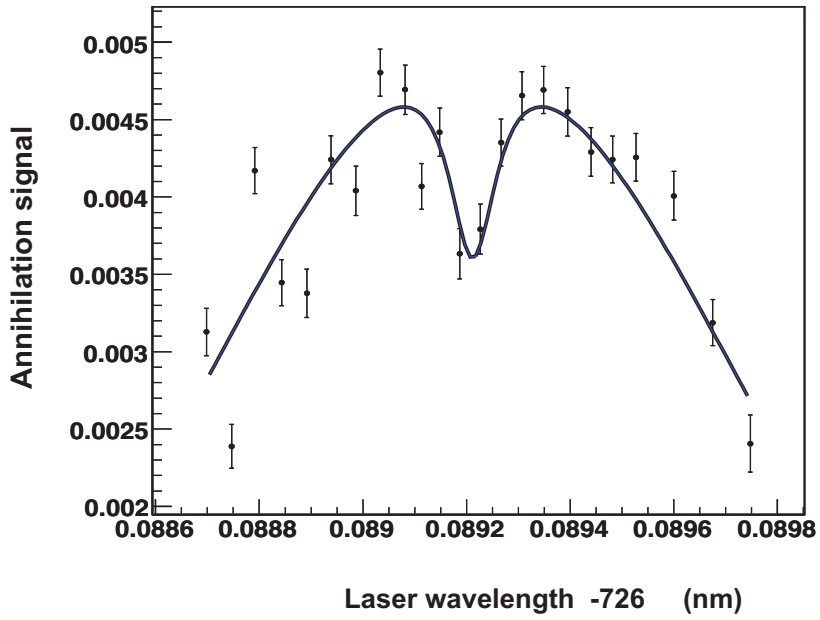

Figure 4: *Resonance profile measured by Doppler-free saturation spectroscopy on the transition* $(37,35)\rightarrow(38,34)$ *of* $\bar{p}^4He^+$ *at wavelength* 726 *nm in 2009. The first laser pulse produces the Lamb dip in the thermal distribution, which is then probed by the second beam. Afterwards three successive power failures occurred in AD and the beam intensity became low and unstable for several weeks. We could not reproduce the result.*

One possible way to improve the experimental precision of $\nu_{\rm exp}$ is to cancel the thermal Doppler broadening of the resonance lines by saturation spectroscopy. This method involved irradiating the $\overline{p}^4{\rm He}^+$ with two counter-propagating laser pulses of the same wavelength $\lambda = 726$ nm. The first laser drove the transition $(n,\ell) = (37,35)\rightarrow(38,34)$ and created a Lamb dip in the thermal distribution of $\overline{p}{\rm He}^+$, which was then probed by the second laser. The first-order Doppler width $\Delta\nu$ is in principle completely canceled.

In 2009, we used the new dye laser to produce 30-ns-long laser pulses of $\lambda = 726$ nm. This beam was split into two beams of energy ~ 2 mJ, which where successively sent into the experimental target in an anti-collinear, counter-propagating geometry. The first laser irradiated the atom $\delta t \sim 50$ ns before the second one. In Fig. 4, the experimental results are shown. The intensity of the antiproton annihilation signal induced by the second laser is plotted as a function of the laser wavelength. A dip appeared in the expected frequency position. Fitting by the theoretically-expected profile yielded a $\nu_{\rm exp}$ value with a slightly higher experimental precision compared to previous single-photon measurements [2]. After this measurement, however, the AD and PS complex suffered three power outages and the antiproton intensity became half of nominal values. Large fluctuations in the position and intensity of the beam prevented us from reproducing these results. We intend to improve this experiment and attempt it again beyond year 2010.

1.3 Precise measurements of the lifetimes of $\overline{p}\mathrm{He}^+$ states

In the above derivation of the electron-to-antiproton mass ratio, the ν_{th}-values are obtained from calculations of the complex energies of $\overline{p}\mathrm{He}^+$ states [3],

$$E_c = E_r - i\frac{\gamma/2\pi}{2}, \tag{2}$$

wherein E_r denotes the real part of the level energy, and γ its decay rate. It is important to compare the γ-values with experimental decay rates to evaluate the overall precision of E_c used to derive $m_e/m_{\overline{p}}$. For this reason in 2008–2009, we systematically measured the Auger rates γ_A of six $\overline{p}\mathrm{He}^+$ states by laser spectroscopy.

States with large $\gamma_A > 10$ GHz Auger rates provide a particularly stringent evaluation of the three-body wavefunction. The decay rates can in principle be derived by exciting laser transitions of the type $(n,\ell)\rightarrow(n+1,\ell-1)$ and measuring the natural width of the resonance profiles. Systematic measurements were carried out in 2004 [14]. Most of the experimental results were within 10–20% of the calculated values, but four states appeared to have decay rates between 3 and 100 times larger than the theoretical ones. Fig. 5 (top) shows the resonance profiles of the $\overline{p}^4\mathrm{He}^+$ transition $(34,33)\rightarrow(35,32)$ (left) and the $\overline{p}^3\mathrm{He}^+$ transition $(33,32)\rightarrow(34,31)$ (right) obtained in the 2004 experiment. This measurement was hampered by the large linewidth ~ 1 GHz of the laser which broadened the spectral resolution and lowered the signal-to-noise ratio. The spectra for the $(34,33)\rightarrow(35,32)$ resonance is particularly poor due to the small transition probability.

In 2009, we remeasured the decay rates of six states $(n,\ell) = (38,33)$, $(37,33)$, and $(35,32)$ in $\overline{p}^4\mathrm{He}^+$, and $(37,32)$, $(36,32)$, and $(34,31)$ in $\overline{p}^3\mathrm{He}^+$ using the new laser with a linewidth ~ 100 times narrower than before. The new spectra in Fig. 5 (bottom) has a much higher signal-to-noise ratio and statistical error compared to the 2004 results. A two-peak structure arising from the hyperfine interaction between the antiproton's orbital angular momentum and electron spin was resolved for the first time. All measured Auger rates γ_A now agree with theoretical calculations within the experimental errors of $10-25\%$.

Another interesting observation was that some $\overline{p}\mathrm{He}^+$ states become short-lived by collisions with helium atoms in the experimental target, whereas other states are unaffected. This was one of the important reasons why the γ-values determined from the 2004 results were larger than theoretical ones by factor 3–100. For example, the decay rate of state $(n,\ell) = (34,31)$ in $\overline{p}^3\mathrm{He}^+$ increased from $< 5\times10^9$ s^{-1} to $\sim 10^{11}$ s^{-1} as the target pressure was changed from $P\sim 100$ mb to 1 Bar at $T\sim 6$ K. On the other hand, state $(35,32)$ of $\overline{p}^4\mathrm{He}^+$ retained a constant decay rate $\sim 6\times10^9$ s^{-1} even up to 1.8 Bar. This collisional shortening of the state lifetimes may be caused by couplings between certain metastable $\overline{p}\mathrm{He}^+$ states with electronically-excited $\overline{p}\mathrm{He}^+$ states. We are currently carrying out theoretical calculations to better understand this effect.

1.4 Plans for 2010 - Spectroscopy of very cold $\overline{p}\mathrm{He}^+$ atoms

In 2009, we measured four transitions in $\overline{p}^3\mathrm{He}^+$ and the ν_{exp} values were within 10–15 parts per billion of ν_{th}. These measurements must be extended to all 12 transitions of both $\overline{p}^4\mathrm{He}^+$ and $\overline{p}^3\mathrm{He}^+$ if we are to derive a new value for the electron-to-antiproton mass ratio. We plan to do this in 2010. The experimental precision will be further improved by cooling the experimental target to temperature $T\sim 1.8$ K, thereby reducing the thermal Doppler width of the resonances by factor ~ 3 compared to now.

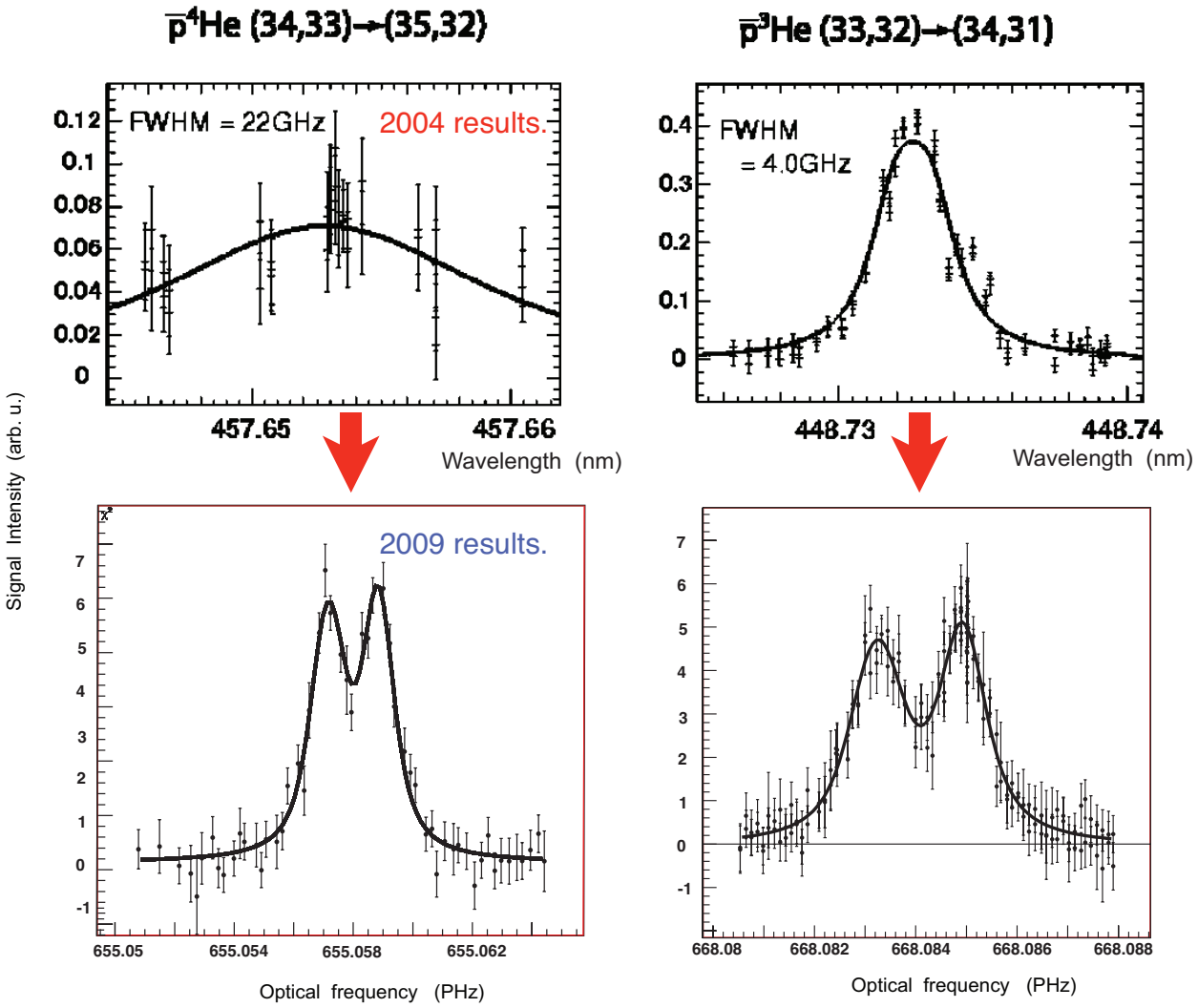

Figure 5: *Resonance profiles of the* $\bar{p}^4\mathrm{He}^+$ *transition* $(34,33)\rightarrow(35,32)$ *(left) and the* $\bar{p}^3\mathrm{He}^+$ *transition* $(33,32)\rightarrow(34,31)$ *(right) measured in 2004 (top) and 2009 (bottom). Note large improvement of the signal-to-noise ratio, statistical error, and spectral resolution due to the improved laser system.*

2 Spectroscopy of the Hyperfine Structure of Antiprotonic Helium

2.1 Introduction

A precise measurement of the antiprotonic helium ($\bar{\mathrm{p}}\mathrm{He}^+$) [15–18] *hyperfine structure* (HFS) can be compared with three-body Quantum Electrodynamic (QED) calculations [19, 20] as a test of their predictions. The HFS of the $(n,L) = (37, 35)$ state of $\bar{\mathrm{p}}^4\mathrm{He}^+$ has now been thoroughly measured [21–23] in terms of the energy eigenvalues. Recent results have reduced the statistical error associated with the individual transitions $\nu^{\pm}_{\mathrm{HF}}$, shown as wavy line in Fig. 7, to a factor of 20 higher precision than that of initial calculations [23]. This has motivated Korobov and Zhong [24] to improve their calculations by adding $m\alpha^6$ order corrections to the electron spin – $\bar{\mathrm{p}}$ orbital angular momentum term E_1 (cf. section 2.2). Their new results for $\nu^{\pm}_{\mathrm{HF}}$ are a factor 3 more precise than before and agree with our latest results [23]. The difference $\Delta\nu_{\mathrm{HF}} = \nu^{-}_{\mathrm{HF}} - \nu^{+}_{\mathrm{HF}}$, which only depends on the coefficients $E_2 \ldots E_4$, has been resolved to a precision comparable to that of

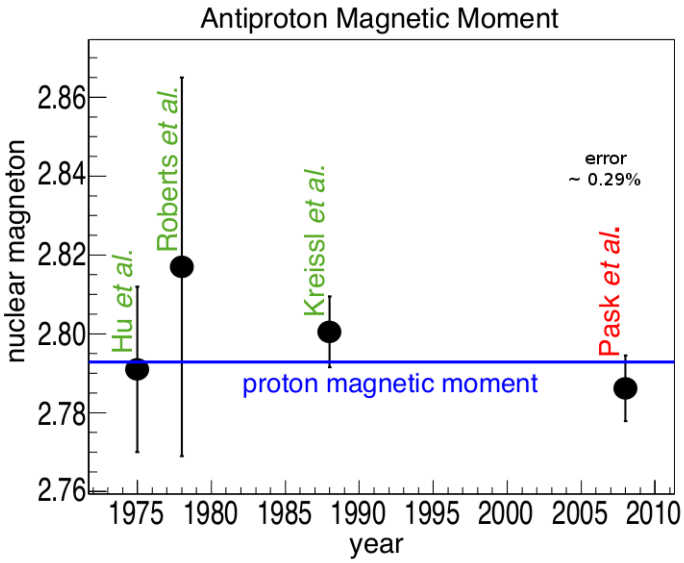

Figure 6: Determination of the magnetic moment of the antiproton as a function of time. Hu *et al.*: [26], Roberts *et al.*: [27], Kreissl *et al.*: [25], Pask *et al.*: [23].

theory (33 kHz), a factor of 10 improvement over our first measurement [21]. A study of the collisional relaxation processes was commenced [22] but could not be completed due to lack of time. As the value of the cross sections for spin-flip collisions is of interest to theory, further measurements of this quantity are still needed.

If they agree, a comparison between the measured transition frequencies and three body QED can be used to determine the antiproton spin magnetic moment $\mu_s^{\bar{p}}$. Such a comparison between the proton and antiproton can be used as a test of CPT invariance. The most precise measurement of the proton to antiproton spin magnetic moment ratio to date is 0.3% [25]. This is illustrated in comparison to previous measurements in Fig. 6. Our new measurements of $\nu_{\rm HF}^{\pm}$ agree with the theoretical values within the calculation error of $\sim 3\times10^{-5}$ = 0.4 MHz [24]. It should be noted that the experimental errors are $\sim$ 60 kHz. The difference between theory and experiment $\Delta_{\rm th-exp}$ is at the $\sim$ 400 kHz level, just about the size of the theoretical error. There is also good agreement between experiment and theory for $\Delta\nu_{\rm HF}$, which is proportional to the spin magnetic moment of the antiproton.

In 2009, a proceedings paper from the LEAP08[3] conference [28] and a final publication summarizing our measurements of the $(37,35)$ state of $\bar{\rm p}^4$He [23] was published. By comparing the measured and calculated [20] value of $\Delta\nu_{\rm HF}$ and taking into account the sensitivity of $\Delta\nu_{\rm HF}$ on $\mu_s^{\bar{p}}$ [29], a new experimental value of the spin magnetic moment of the antiproton was obtained as

$$\mu_s^{\bar{p}} = -2.7862(83)\mu_N, \tag{3}$$

slightly better than the previously best measurement [25] which so far dominates the PDG value [11]. Comparison to the proton magnetic moment μ_s^p gives

$$\frac{\mu_s^p - |\,\mu_s^{\bar{p}}\,|}{\mu_s^p} = (2.4 \pm 2.9)\times10^{-3}. \tag{4}$$

[3]Low Energy Antiproton Physics, Vienna, Austria

The precision achieved for the (37, 35) state in $\overline{\mathrm{p}}^4\mathrm{He}^+$ cannot be improved further due to fluctuations of the $\overline{\mathrm{p}}$ beam. Therefore a first measurement of $\overline{\mathrm{p}}^3\mathrm{He}^+$ has been proposed which can be performed with a similar experimental set up. We have received FWF[4] funding (proposal number I-198-N20) for this three year project.

In 2009, the measurement of a new state has been started: the (n,L) = (36, 34) state of $\overline{\mathrm{p}}^3\mathrm{He}^+$. $\overline{\mathrm{p}}^3\mathrm{He}^+$ is a more complex system than $\overline{\mathrm{p}}^4\mathrm{He}^+$ as described in Section 2.2. A comparison between the theoretical calculations and experimental results would lead to a more rigorous test of the theory and address any systematic errors therein. A measurement of this state would be the first HF measurement on $\overline{\mathrm{p}}^3\mathrm{He}^+$. This year, a significant signal could not yet be observed. A thorough analysis of the problems is being done and the experimental setup will undergo the necessary improvements, promising to observe a significant signal during the beamtime 2010.

2.2 Hyperfine Structure

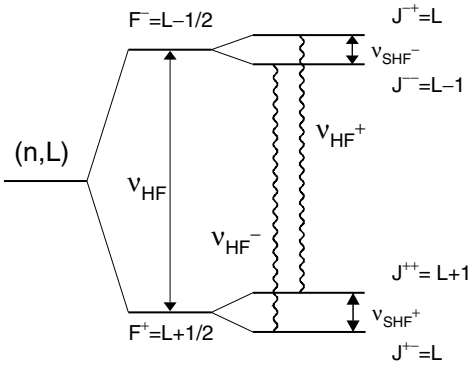

Figure 7: Hyperfine splitting (HFS) *of a state* (n,L) *of* $\overline{\mathrm{p}}^4He^+$. *The wavy lines denote allowed M1 transitions that can be stimulated by microwave radiation.*

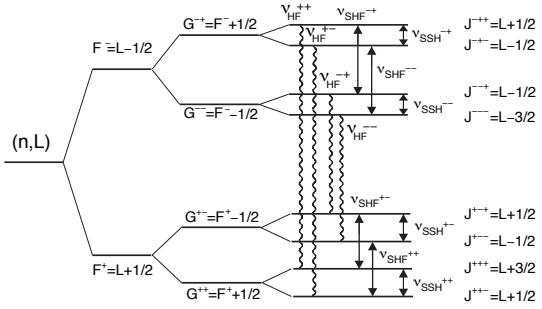

Figure 8: Hyperfine splitting (HFS) *of a state* (n,L) *of* $\overline{\mathrm{p}}^3He^+$. *The wavy lines denote allowed M1 transitions that can be stimulated by microwave radiation.*

The HFS of $\overline{\mathrm{p}}\mathrm{He}^+$ arises from the interaction of the magnetic moments of its constituents and has been calculated by Korobov and Bakalov to α^4 order [19, 20][5] They constructed an effective Hamiltonian for $\overline{\mathrm{p}}^4\mathrm{He}^+$

$$H^{\mathrm{eff}} = E_1(\vec{L}\cdot\vec{S}_{\mathrm{e}}) + E_2(\vec{L}\cdot\vec{S}_{\overline{\mathrm{p}}}) + E_3(\vec{S}_{\mathrm{e}}\cdot\vec{S}_{\overline{\mathrm{p}}})$$

$$+E_4\{2L(L+1)(\vec{S}_{\mathrm{e}}\cdot\vec{S}_{\overline{\mathrm{p}}}) - 6[(\vec{L}\cdot\vec{S}_{\mathrm{e}})(\vec{L}\cdot\vec{S}_{\overline{\mathrm{p}}})]\}. \quad (5)$$

Due to the large orbital angular moment of the antiproton ($\vec{L}\sim 35$), the dominant splitting arises from the interaction of $\sim\vec{L}$ with the electron spin $\vec{S}_{\mathrm{e}}$. The antiproton spin $\vec{S}_{\overline{\mathrm{p}}}$ and the spin $\vec{S}_{\mathrm{h}}$ of the 'helion' h, the ^{3}He nucleus, lead to further splittings leading to a quadruplet for $\overline{\mathrm{p}}^4\mathrm{He}^+$ and an octet for $\overline{\mathrm{p}}^3\mathrm{He}^+$. The effective Hamiltonian for $\overline{\mathrm{p}}^3\mathrm{He}^+$ is more complicated and contains nine terms [30].

In Fig. 7 and Fig. 8 the allowed M1 transitions that can be induced by an oscillating magnetic field are shown. In the case of $\overline{\mathrm{p}}^4\mathrm{He}^+$, there are two types of transitions: HF transitions (ν_{HF}^+ and ν_{HF}^-) which are

[4] Austrian Science Fund

[5] Recently the E_1 term has been calculated by Korobov and Zhong [24] to $m\alpha^6$ order for the $(n,L) = (37,35)$ state of $\overline{\mathrm{p}}^4\mathrm{He}^+$ only.

associated with a spin-flip of the electron, and *superhyperfine (SHF)* transitions ($\nu^{+}_{\rm SHF}$ and $\nu^{-}_{\rm SHF}$) which are associated with a spin flip of the antiproton.

In the case of $\overline{\rm p}^3{\rm He}^+$, there is an additional transition. The HF transitions are still associated with the spin flip of the electron ($\nu^{++}_{\rm HF}$, $\nu^{+-}_{\rm HF}$, $\nu^{-+}_{\rm HF}$ and $\nu^{--}_{\rm HF}$). Although the helion magnetic moment is smaller than that of the antiproton, its overlap with the electron cloud (which is in the ground state and has its maximum probability at the helion site) is stronger. Therefore the helion spin contributes to the quadruplet superhyperfine splitting ($\nu^{-+}_{\rm SHF}$, $\nu^{--}_{\rm SHF}$, $\nu^{+-}_{\rm SHF}$ and $\nu^{++}_{\rm SHF}$) and *super-superhyperfine (SSHF)* transitions are caused by the spin flip of the antiproton ($\nu^{-+}_{\rm SSHF}$, $\nu^{--}_{\rm SSHF}$, $\nu^{+-}_{\rm SSHF}$ and $\nu^{++}_{\rm SSHF}$) [17].

The hierarchy of angular moments and the angular momentum coupling schemes are shown in Tables 1 and 2 (numerical values from CODATA2002; $\mu\overline{\rm p} = -2.800(8)\mu_N$ (PDG)):

Table 1: *Hierarchy of angular momenta, where $\mu_B = {\rm e}\hbar/2{\rm m_e}$ is the Bohr magneton, $\mu_N = {\rm e}\hbar/2{\rm m_{\overline{p}}}$ is the nuclear magneton and g is the giromagnetic ratio.*

$\vec{\mu}_{\rm e} = g_e\mu_B\vec{S}_{\rm e}$	= -1.001 159 652 1859(38)μ_B
$\vec{\mu}^{l}_{\overline{\rm p}} = g^{\overline{\rm p}}_{l}\mu_N\vec{L}_{\overline{\rm p}}$	$\sim$ 1.906 159 $\times 10^{-2}\mu_B$
$\vec{\mu}^{s}_{\overline{\rm p}} = g^{\overline{\rm p}}_{s}\mu_N\vec{S}_{\overline{\rm p}}$= 2.792 847 351(28) $\mu_N(p)$	= 1.521 032 206(15) $\times\ 10^{-3}\mu_B$
$\vec{\mu}_{h} = g_{\rm h}\mu_N\vec{S}_{\rm h}$= -2.127 497 723(25) μ_N	= -1.158 671 474(14)$\times\ 10^{-3}\mu_B$

Table 2: *Angular momentum couplings where HFS is the hyperfine structure, SHFS is the super hyperfine structure and SSHFS is the super super hyperfine structure.*

	$\overline{\rm p}^4{\rm He}^+$	$\overline{\rm p}^3{\rm He}^+$
HFS	$\vec{F} = \vec{L}_{\overline{\rm p}} + \overrightarrow{S}_{\rm e}$	$\vec{F} = \vec{L}_{\overline{\rm p}} + \vec{S}_{\rm e}$
SHFS	$\vec{J} = \vec{F} + \vec{S}_{\overline{\rm p}} = \vec{L}_{\overline{\rm p}} + \vec{S}_{\rm e} + \vec{S}_{\overline{\rm p}}$	$\vec{G} = \vec{F} + \vec{S}_{\rm h} = \vec{L}_{\overline{\rm p}} + \vec{S}_{\rm e} + \vec{S}_{\rm h}$
SSHFS		$\vec{J} = \vec{G} + \vec{S}_{\overline{\rm p}} = \vec{L}_{\overline{\rm p}} + \vec{S}_{\rm e} + \vec{S}_{\rm h} + \vec{S}_{\overline{\rm p}}$

The transitions between the SSHF octets of $\overline{\rm p}^3{\rm He}^+$ can be measured with the same method as those between the SHF quadruplets of $\overline{\rm p}^4{\rm He}^+$. Instead of two transitions, shown in Fig. 7), there are now four as shown in Fig. 8). The most appropriate candidate state is the (n,L) = (36, 34) state, which has an unfavoured laser transition to (37, 33) of $\sim$ 724 nm, close to that of the previous measurement ($\sim$ 726 nm). Korobov and Bakalov calculate the microwave transitions as the following [30],

16 GHz transitions:

$$J^{+++} = L + \frac{3}{2} \mapsto J^{-++} = L + \frac{1}{2} = 16.1107\,{\rm GHz} \tag{6}$$

$$J^{++-} = L + \frac{1}{2} \mapsto J^{-+-} = L - \frac{1}{2} = 16.1434\,{\rm GHz} \tag{7}$$

Difference = 32.72 MHz

11 GHz transitions:

$$J^{+-+} = L + \frac{1}{2} \mapsto J^{--+} = L - \frac{1}{2} = 11.1250\,{\rm GHz} \tag{8}$$

$$J^{+--} = L - \frac{1}{2} \mapsto J^{---} = L - \frac{3}{2} = 11.1577{\rm GHz} \tag{9}$$

Difference = 32.73 MHz

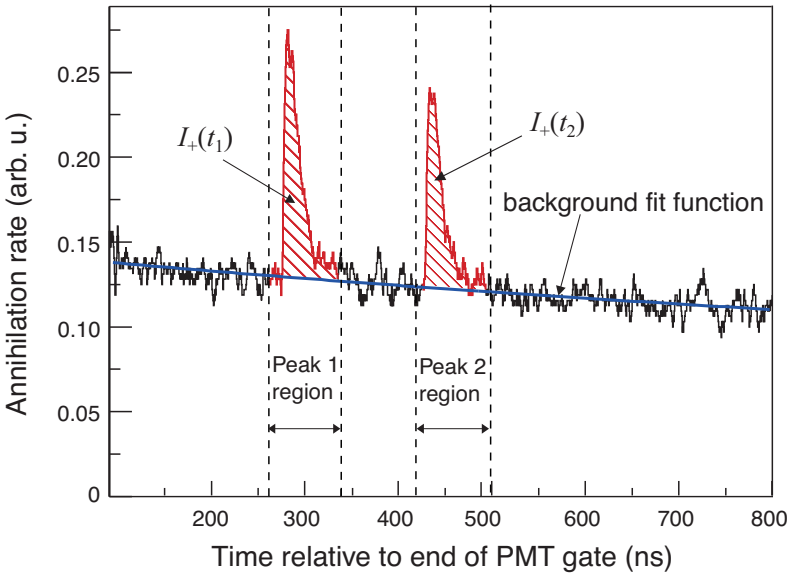

Figure 9: *Two laser stimulated annihilation peaks against the exponential decaying background of the other state populations. The peak-to-total of each is calculated by taking the ratio of the peak area (I_+) to the total area under the full spectrum.*

2.3 Experimental Method

The laser spectroscopy method takes advantage of the charged pions produced when the antiproton annihilates in the helium nucleus. An exponentially decaying background signal is ever present as the antiprotons, in various levels of the cascade, decay and eventually annihilate in the nucleus. This is referred to as an *analog delayed annihilation time spectrum (ADATS)*, analog because a voltage proportional to the number of events is recorded. A measurement of a particular state can be made by laser stimulated transfer to a fast-decaying, Auger decay dominated, daughter state. The ratio of the peak area to the total background area (peak-to-total) indicates the size of the population transferred from the parent to the daughter state.

A microwave pulse can be used to transfer the populations between SSHFS octet states via an electron spin flip. Combined with the laser, to make a laser-microwave-laser technique, this method can be used to measure the transition frequencies.

Initially all the octet states are equally populated and so a population asymmetry must first be induced. A narrow band laser pulse, tuned to the f^+ transition, creates this asymmetry. The J^{+-+}, J^{+--}, J^{+++} and J^{++-} octet states are depopulated through a laser induced transfer to the Auger dominated decay state, while the J^{-++}, J^{-+-}, J^{--+} and J^{---} octet states remain relatively unaffected. This produces the first peak shown in Fig. 9. The microwave envelope follows which, if on resonance, results in partially inverting the asymmetry: refilling either the J^{+-+} or J^{+--} from the J^{--+} or J^{---} octet state in the $\sim$ 11 GHz region or the J^{+++} or J^{++-} from the J^{-++} or J^{-+-} octet state in the $\sim$ 16 GHz region respectively. After refilling, a second laser pulse, tuned to the same f^+ transition, is used to depopulate the doublet state again, producing the second peak shown in Fig. 9.

The first laser-induced annihilation peak remains constant, fluctuating only statistically or with the varying conditions of the target, and is therefore used to normalise the second. The second annihilation peak corresponds directly to the population transferred between the hyperfine substates by the microwave. The microwave frequency is scanned across the expected resonant frequency. A plot of the microwave frequency vs the normalised second annihilation peak, produces a peak at the resonant frequency.

2.4 Experimental Apparatus

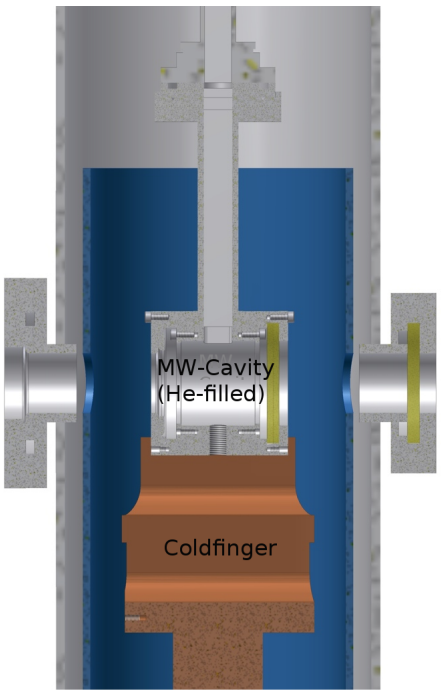

Figure 10: *A drawing of the new cryostat.*

Figure 11: *Photographs of the new cavity mounted on the coldhead.*

The principle of the new experiment with $\overline{\mathrm{p}}^3\mathrm{He}^+$ is the same as that for the $\overline{\mathrm{p}}^4\mathrm{He}^+$ (37, 35) state measurements. Therefore the required apparatus essentially remained the same, except for the cavity and cryostat where we developed a completely new hermtically sealed cavity cooled by a liquid-helium free cryostat. The microwave setup is described in detail by Sakaguchi *et al.* [31] while the laser system is described in Hori *et al.* [32] and summarised in Pask *et al.* [22]. The laser transition between the parent state $(n, L) = (36, 34)$ and the Auger decay dominated state (37, 33) is $\sim$ 724 nm so an identical laser system can be used.

A new cavity for the $\sim$ 11 GHz transitions and a new cryostat with a compressor-based cooling system have been designed and built in Vienna, see Fig. 10 and Fig. 11. Further a new microwave signal generator and amplifier have been used for the 2009 measurements. To produce a $\sim$ 16 GHz microwave signal will require also new waveguides. Therefore, it was proposed to measure the 11 GHz transition in 2009 and the 16 GHz in 2010.

2.5 2009 Measurements

In 2009 we tried to measure the (36, 34) state in $\overline{\mathrm{p}}^3\mathrm{He}^+$ for the first time, using the same experimental method but a new setup. Our aim was to test the new setup and study two of the four SSHF transitions in $\overline{\mathrm{p}}^3\mathrm{He}^+$. The new cryostat (see Figs. 10, 11) worked successfully. It could be kept very stable at a pressure up to more than 1 bar and the cavity temperature stabilized within minutes. The laser system worked fine and we could verify the theoretical predictions for the laser splitting with very good resolution, which is illustrated by the laser scan in Fig. 12. The hyperfine structure consisting of two laser transitions with larger separation (left peak) and two transitions with very small separation (right peak) agrees with the theoretical predictions and previous measurements [32]. The achieved laser depletion efficiency was even higher than for $\overline{\mathrm{p}}^4\mathrm{He}^+$, in agreement with the shorter Auger lifetime of the (37,33) daughter state.

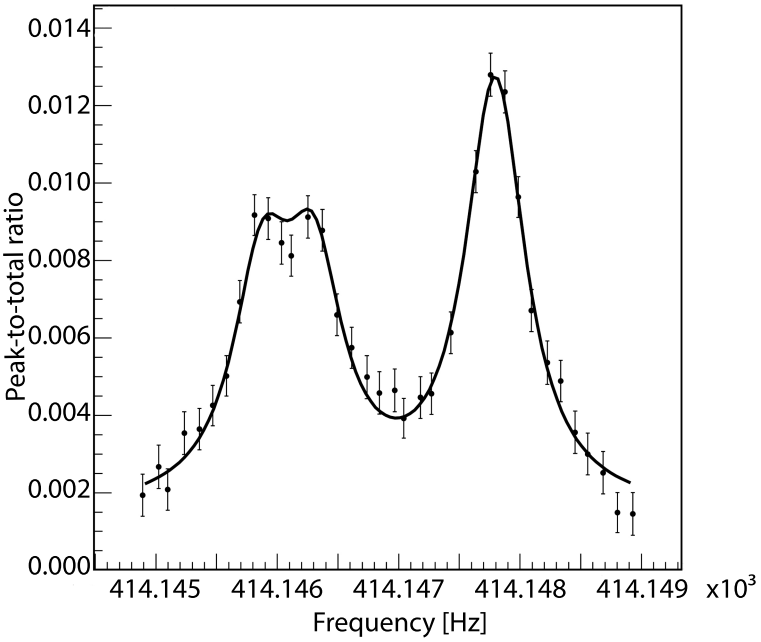

Figure 12: *A laser scan for the (36, 34) → (37, 33) transition in* $\overline{p}^3He^+$

Unfortunately we could not yet succeed in observing a microwave transition signal. The electric dipole moments of the (36, 34) → (37, 33) transition in $\overline{p}^3He^+$ are of the same order as those of the measured transition in $\overline{p}^4He^+$. However, the presence of twice as many HF states increases the background and therefore has the potential to reduce the relative signal, according to preliminary simulations to about 10%. Therefore, the measurements are very sensitive to fluctuations of the antiproton or the laser beam and it is crucial to accumulate enough statistics to see a significant, reproducible signal. The beam extraction to the ASACUSA beamline was not good for considerable time, even though the provided antiproton intensity was very good this year. Problems with new electronic equipment caused additional delay through time consuming changes. The main difficulties may have been caused by the new microwave setup, i.e. the system of cavity and waveguides. It is possible that the power or the field mode inside the microwave cavity were not as we expected during the measurements. If these characteristics were different, that would explain why we did not observe a signal. RF experts have been consulted for advise and extensive investigation is being done now to improve the setup.

2.6 Proposed Measurements in 2010 and Beamtime Request

The beamtime will be divided essentially in two parts. We are planning to measure the (37, 35) state in $\overline{p}^4He^+$ again for two reasons: a verification of the measurement of this already extensively investigated transition with the new experimental setup would exclude a problem due to the setup. The major motivation is to finish a study on collisional relaxations which could not yet be completed due to insufficient statistics. These measurements require to build a new cavity, which can be mounted within the new cryostat, and some minor modifications to allow for changing the cavity within one day. In the second part it is planned to measure the $\overline{p}^3He^+$ transitions at 11 GHz with an improved setup. We aim to measure at least at three different target densities (150 mbar, 250 mbar and 500 mbar). The density dependence of the laser transitions varies strongly with the state and thus a density dependent study should also be made of the new state in

$\bar{p}^3He^+$.

Since for the measurements of the $\bar{p}^4He^+$ transition the expected signal height and the required microwave power are already well known, it is assumed to proceed quickly to the actual measurement of the microwave induced SSHF transitions. This is not the case for the new state in $\bar{p}^3He^+$, where an extensive study of the correct microwave power and the microwave signal, obtained from the laser annihilation rate(s), will be necessary. Another crucial point is the accumulation of enough statistics, which is also a time intense process.

3 Cusp trap experiment for $\bar{H}$ synthesis and ground-state hyperfine spectroscopy

Figure 13 shows a layout of the experimental setup for the cusp trap $\bar{H}$ experiment in 2009, which consists of the MUSASHI (Mono-energetic Ultra Slow Antiproton Source for High-precision Investigations) antiproton ($\bar{p}$) accumulator, the cusp trap, and the positron (e^+) accumulator (from left to right). $\bar{p}$s and e^+s are injected into the Cusp trap from the MUSASHI $\bar{p}$ accumulator and the e^+ pre-accumulator, respectively. The Cusp trap is to synthesize antihydrogen atoms ($\bar{H}$s) and to yield spin-polarized $\bar{H}$ beam [33]. It consists of anti-Helmholtz coils which generates a so-called Cusp magnetic field and a multi-ring trap (Cusp-MRT) to generate a multipole electric field.

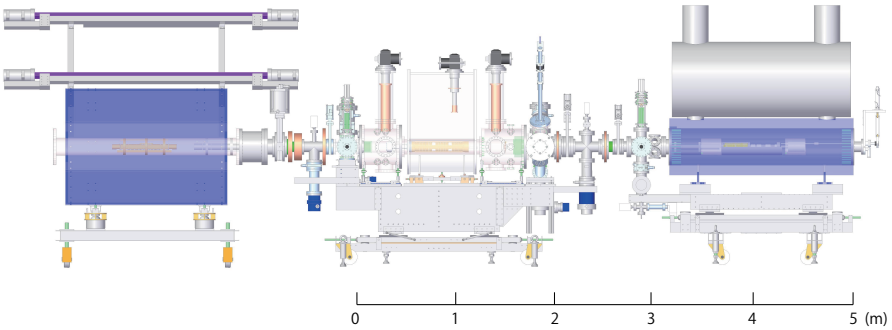

Figure 13: *Layout of the cusp trap $\bar{H}$ experiment, which consists of the MUSASHI $\bar{p}$ accumulator, the Cusp trap and the Positron accumulator (from left to right).*

3.1 Status of the MUSASHI $\bar{p}$ accumulator

Mono-energetic antiproton beams of several tens eV are efficiently prepared by the MUSASHI accumulator, which traps several tens keV $\bar{p}$s from the AD via the RFQD [34], and then cools and manipulates $\bar{p}$s. In 2009, the MUSASHI accumulator provided a 20–30 s long "DC-like" 250 eV $\bar{p}$ beam, and also a 150 eV 2 μs pulse beam. The AD achieved a record high beam intensity of 4×10^7 $\bar{p}$ per AD shot in 2009, which also resulted in the highest trapped number of $\bar{p}$s, 1.9×10^6 per AD shot in the MUSASHI accumulator [6].

The extraction efficiency of ultraslow $\bar{p}$ beams from the MUSASHI accumulator was smaller than that in 2008 except for the first week of the MUSASHI beamtime. The overall extraction fraction against the trapped $\bar{p}$s became $\sim 1/3$, which is a half of the best record in the past. The cause of this efficiency drop is under investigation, and the problem will be fixed during this winter shutdown.

[6] On the other hand, we often experienced difficulties in tuning AD beams due to orbit jumps

We found that the extraction efficiency increased by stacking the AD shots. This is primarily because the radial compression of $\bar{p}$ cloud gets more efficient with more antiprotons, which indicates that we are realizing $\bar{p}$ plasma for the first time [35]. Further details will be studied in 2010.

3.1.1 Tank Circuit Monitoring of Antiprotons in MUSASHI accumulator

We applied a tank circuit technique [36, 37] to monitor accumulated $\bar{p}$s non-destructively. Figure 14 shows a schematic drawing of the experimental setup, which consisted of a variable capacitor and an inductor attached to one of ring electrodes of the MUSASHI trap [38]. The amplified signal is monitored with a spectrum analyzer as shown in fig.14.

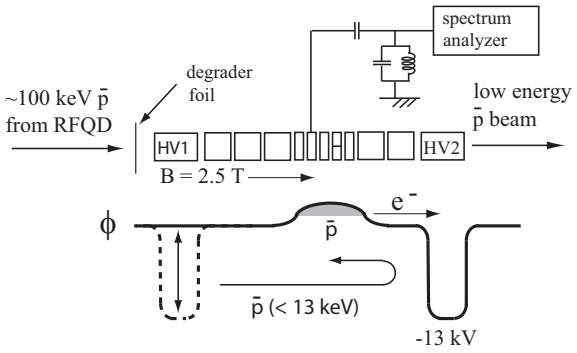

Figure 14: *A schematic drawing of the experimental setup for the non-destructive monitoring of a $\bar{p}$ cloud in the MUSASHI-MRT. $\bar{p}$s of ∼10keV are injected and cooled with pre-loaded electrons. After cooling, the electrons are kicked out, and the tank circuit attached to one of the ring electrodes observe a signal of $\bar{p}$s.*

Signals from the tank circuit provide information on the trapped $\bar{p}$s like Schottky signals from high energy beams in accelerators. In fact, it is known that this kind of trap-based beams [39] are physically equivalent with those in a FODO lattice [40, 41].

3.1.2 Analogy between a FODO lattice and a trap

Here, the analogy between a non-neutral plasma in a solenoid trap and a charged particle beam in a FODO lattice is briefly reviewed [39]. When charged particles (mass : m, charge : e) are confined in an infinitely long uniform magnetic field B in z direction, the Hamiltonian H_{sol} of a test particle, which describes the motion in $x-y$ plane, is given by

$$H_{sol} = \frac{1}{2m}\left[\left(p_x + \frac{eBy}{2}\right)^2 + \left(p_y + \frac{eBx}{2}\right)^2\right] + e\phi_{sc},$$

where ϕ_{sc} is the electric potential due to the space charge of the charged particles. In the rotating frame of reference around the z-axis (with the angular frequency of $eB/2m$), the Hamiltonian, $\tilde{H}_{sol}$, is given by

$$\tilde{H}_{sol} = \frac{\tilde{p_x}^2 + \tilde{p_y}^2}{2} + \frac{1}{2}K_3(\tilde{x}^2 + \tilde{y}^2) + \frac{e}{mc^2}\tilde{\phi_{sc}}. \tag{10}$$

The energy and momentum are normalized by mc^2 and mc, respectively and $K_3 = (eB/2mc)^2$. The quantities with tilde are those in the rotating frame.

Since the Hamiltonian H_{beam} of a test particle in a periodic focusing channel can be approximated with

$$H_{beam} \approx \frac{p_x^2 + p_y^2}{2} + \frac{1}{2}K_1(z)(x^2 - y^2) + \frac{e}{p_0\beta_0 c\gamma_0^2}\phi_{sc},$$

a clear correspondence is seen between the two systems. Under the smooth focusing approximation of the periodic focusing channel, both systems are physically equivalent with each other.

Assuming the Kapchinsky-Vladimirsky distribution (a uniform density distribution in the phase space) for the charged particles, with a circular cross section having radius a and density n, the self field potential $\phi_{sc} = -\frac{en}{4\varepsilon_0}(\tilde{x}^2 + \tilde{y}^2)$ can be substituted into eq.(10), which yields

$$\tilde{H}_{sol} = \frac{\tilde{p_x}^2 + \tilde{p_y}^2}{2} + \frac{1}{2}\left(K_3 - \frac{K_s}{a^2}\right)(\tilde{x}^2 + \tilde{y}^2), \tag{11}$$

where $K_s = \frac{\pi a^2 n e^2}{2\pi\varepsilon_0 mc^2}$. The radius a satisfies the envelope equation below,

$$a' + K_3 a - \frac{K_s}{a} - \frac{\varepsilon^2}{a^3} = 0.$$

Then, the space-charge limit condition is obtained for $K_3 - K_s/a^2 = 0$, which yields $n_{lim} = \varepsilon_0 B^2/2m$ as the maximum density. Also, the bare tune σ_0, space-charge depressed tune σ, and the tune depression of the solenoid system are described as below.

$$\sigma_0 = \frac{eB}{2mc}, \quad \sigma = \sqrt{K_3 - \frac{K_s}{a^2}}, \quad \eta = \frac{\sigma}{\sigma_0} = \sqrt{1 - \frac{n}{n_{lim}}}.$$

Although the above formulation is valid for an infinitely long plasma column, it is also applicable for a uniform density spheroidal plasma confined in a harmonic potential.

3.1.3 Tank circuit signal

Figure 15(a) shows an example of the integrated annihilation events monitored by a track detector placed along the MUSASHI accumulator as a function of time. The first 3 steps seen at $t \sim$150, $\sim$250, and $\sim$390s correspond to the injection of AD shots. Then, electrons for cooling $\bar{p}$s were kicked out and a rotating electric field was applied for 300 s to compress the $\bar{p}$ cloud. At $t \sim$710s, $\bar{p}$s were extracted slowly, which is seen as a large step in fig.15(a). This step size corresponds to $N_{\bar{p}} \sim 4.4 \times 10^6$. Figure 15(b) shows an example of the spectrum analyzer output measured $\sim$30s before the extraction. The strong peak at 256kHz observed in the first 2.5s is the rotating electric field to compress $\bar{p}$s. The noise observed around 683s in fig.15(b) is due to white noise, which was applied to fully kick out small amount of electrons accumulated in the trap through annihilation of $\bar{p}$s with the residual gas (mainly H_2) in the trap. A clear trace of dip is recognized in the spectrum[7]. An example of the power spectrum at $\sim$695 s is shown in fig.15(c). The frequency at the dip corresponds to the axial oscillation frequency of $\bar{p}$s in the MUSASHI-MRT and the dip width reflects $N_{\bar{p}}$. Figure 15(d) shows the relation between the dip width and $N_{\bar{p}}$. We succeeded in non-destructive monitoring of the trapped $\bar{p}$ number with a tank circuit for the first time.

[7]The resonance frequency shifts from 255 kHz to 250 kHz in $\sim$25 s, which is again due to accumulation of electrons produced by $\bar{p}$ annihilation during this period ($\sim 6.6 \times 10^4$).

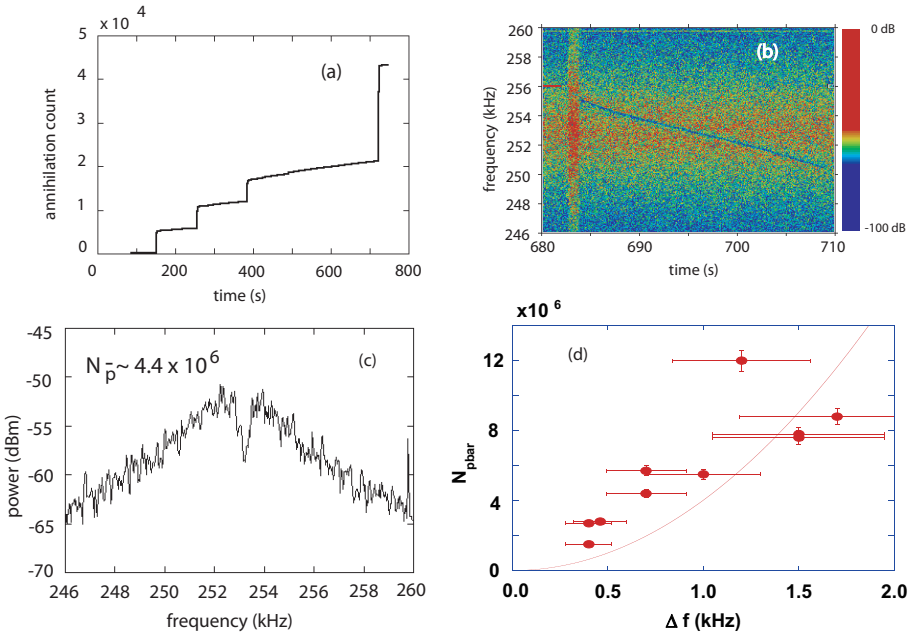

Figure 15: *(a) Integrated counts monitored by a track detector aligned along the MUSASHI trap. Three steps observed at 150s, 250s, and 390s correspond to 3 AD shots. (b) An example of the spectrum analyzer output. Cooling electrons were kicked out by applying white noise at t ∼683s for 1 s. (c) A spectrum of 4.4 × 10^6 antiprotons in the MUSASHI-MRT. (d) The relation between the dip width and the number of $\bar{p}$s.*

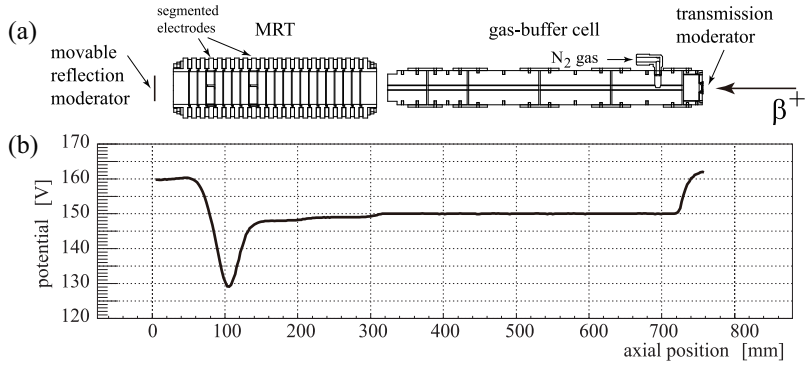

Figure 16: *(a) A Cross-sectional view of the trapping part of the positron pre-accumulator and (b) optimized electric potential along the axis of the trap including two moderators on both ends.*

3.2 Positron pre-accumulator

An exceptionally compact positron pre-accumulator based on the N_2 gas-buffer scheme [42] applicable to the cusp trap was installed in 2008. Large research effort was devoted to improve and optimize the efficiency of the pre-accumulator in 2009.

3.2.1 Efficiency of the pre-accumulator

Figure 16(a) shows a cross-sectional view of the trapping part of the positron pre-accumulator, which consists of a movable reflection moderator, the positron MRT, a pressure gradient gas-buffer cell, a transmission moderator, and the ^{22}Na positron source (from left to right). Both moderators are made of polycrystalline

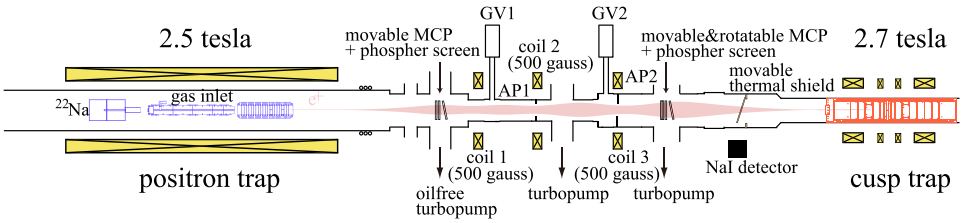

Figure 17: *A schematic view of the transport line between the positron pre-accumulator and the cusp trap. An envelope of calculated positron trajectories from the pre-accumulator to the cusp trap is also shown.*

tungsten (W). The full setup is housed in a 2.5T superconducting solenoid with a cold bore operated at $\sim$100K. The N_2 gas-buffer cell was re-designed (ϕ=6 mm, 400 mm in length) to prepare a proper pressure gradient in the gas cell and the positron MRT. The pressure gradient of N_2 gas and the potential distribution have big impacts on the trapping efficiency. Figure 16(b) shows the optimized potential distribution for the best positron accumulation. Because the length of the trapping region was quite limited in our all-in-one system compared with the conventional large positron accumulators [42], the pressure gradient of the buffer gas in the MRT were sharper. The pseudo-harmonic potential for confining positrons is made at the exit side (left side of fig.16(b)) of the MRT where positrons have the lifetime of $\sim$100s when a proper amount of the buffer gas presents. By this way, the number of positrons trapped in the pre-accumulator was improved more than ten times than that in 2008, and $\sim 2\times10^6$ e^+ were accumulated in 100 s. Although the efficiency of the moderator here has not been measured yet, the expected trapping efficiency assuming a published moderator efficiency of polycrystalline W [43] is more than 25%, which is favorably comparable to the best values of conventional accumulators, i.e., our pre-accumulator reaches almost maximum performance as an accumulator with polycrystalline tungsten moderators.

3.2.2 Positron transport, stacking, and manipulation in the cusp trap

Figure 17 shows a schematic view of the transport line of positrons from the pre-accumulator to the cusp trap. Three guiding coils were prepared to realize high transport efficiency. During accumulation of positrons in the pre-accumulator, the vacuum separation valves (GV1 and GV2) were closed to keep the cusp trap part under ultra high vacuum (UHV) conditions. GV1 and GV2 were opened and the transfer magnet is energized (500 gauss) during the positron transport. The positrons accumulated in the pre-accumulator are extracted as a low-energy ($\sim$100 eV) pulsed beam and transported to the cusp trap via two apertures (AP1 and AP2) for differential pumping. The pulsed positrons are caught in the Cusp-MRT by opening and closing a gate electrode. The number of positrons in the Cusp-MRT and its radial distribution were monitored by an imager consisted of a micro-channel plate (MCP) and a phosphor screen (see fig.17) installed downstream of the Cusp-MRT. NaI and plastic scintillators were used to monitor the number of positrons in the pulse and the pulse width of the extracted positron beam, respectively. The whole experimental operations including the radiation shield movement of the ^{22}Na source, moderator movement, potential manipulation of MRTs, detector movement, the data acquisition from the detectors and controlling the gate valves are automated to realize continuous and remote-controlled experiments. The lifetime of the positrons in the cusp trap was $\sim$6000s, which enabled us to stack sequent shots of positrons from the pre-accumulator. More than ten millions of positrons were accumulated in the Cusp-MRT for $\bar{H}$ recombination experiments.

In order to make high-density positron plasma, the radial distribution of the positron cloud in the Cusp-MRT was compressed using a rotating wall electric field. It was found that the rotating wall compression [44] was effective and reproducible also for positron plasmas in an inhomogeneous cusp magnetic fields, e.g., 2 millions of positrons with a density of 8×10^6 cm^{-3} were compressed to a density of 3×10^8 cm^{-3} in

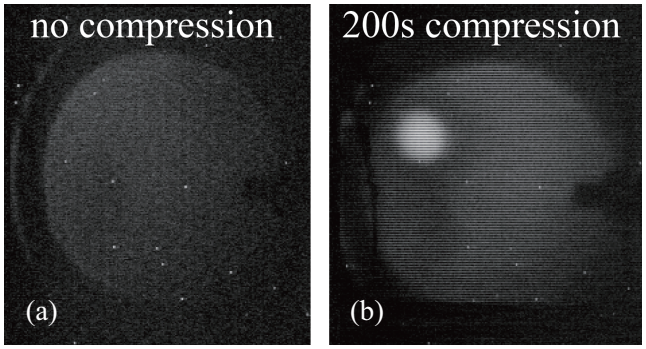

Figure 18: *Positron images on the phosphor screen at the downstream of the cusp trap (a) before and (b) after compression.*

200s. Figure 18(a) and (b) show images of positron cloud monitored by the movable MCP and phosphor screen before and after compression, respectively. Fine adjustment and further improvement of the positron controlling techniques applicable in a wide range of operation parameters are in progress.

3.3 Mixing $\bar{p}$ and e^+ in the Cusp trap

3.3.1 New Cold bore of the Cusp trap

The Cusp-MRT is housed in a cold bore which is cooled by two stages GM-type cryocoolers to reduce the annihilation rate of $\bar{p}$s with residual gas as low as possible [45]. A small cold leak was found last year, which made the $\bar{p}$ life time $\sim$80 s. In order to improve this situation, the cold bore was replaced with a new one, which improved the $\bar{p}$ lifetime several times, i.e., 200–500 s in the Cusp trap.

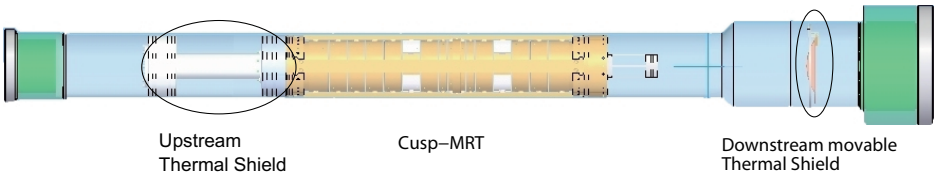

Figure 19: *A schematic view of the Cold bore with the upstream thermal shield, the Cusp-MRT, and the downstream thermal shield (from left to right).*

At the same time, new thermal radiation shields were installed on both ends of the bore tube as shown in fig.19. A thick cylinder with a long tube and a small hole (16 mm in diameter) is prepared at the upstream 30K stage of the bore tube. The hole size is chosen so that it does not affect $\bar{p}$ transport from the MUSASHI accumulator, but reduce the conductance by a factor of 30, 6.4l/s, and the radiation heat load by a factor of 6 as compared with those in 2008. The other shield is a movable disk installed at the downstream of the bore tube, which blocks room temperature radiation as well as gas load. The disk is made of a Au-coated copper and thermally bridged to the 30K stage of the bore tube by silver foils.

3.3.2 $\bar{p}$ annihilation rate with e^+

Figure 20(a) shows a cross-sectional view of the cusp magnet, two thermal shields, and the Cusp-MRT with magnetic field lines superimposed. In order to maximize the number of usable positrons, we tried to synthesize $\bar{\mathrm{H}}$ atoms at the downstream spindle region of the Cusp-MRT. A typical nested potential [46] [47]

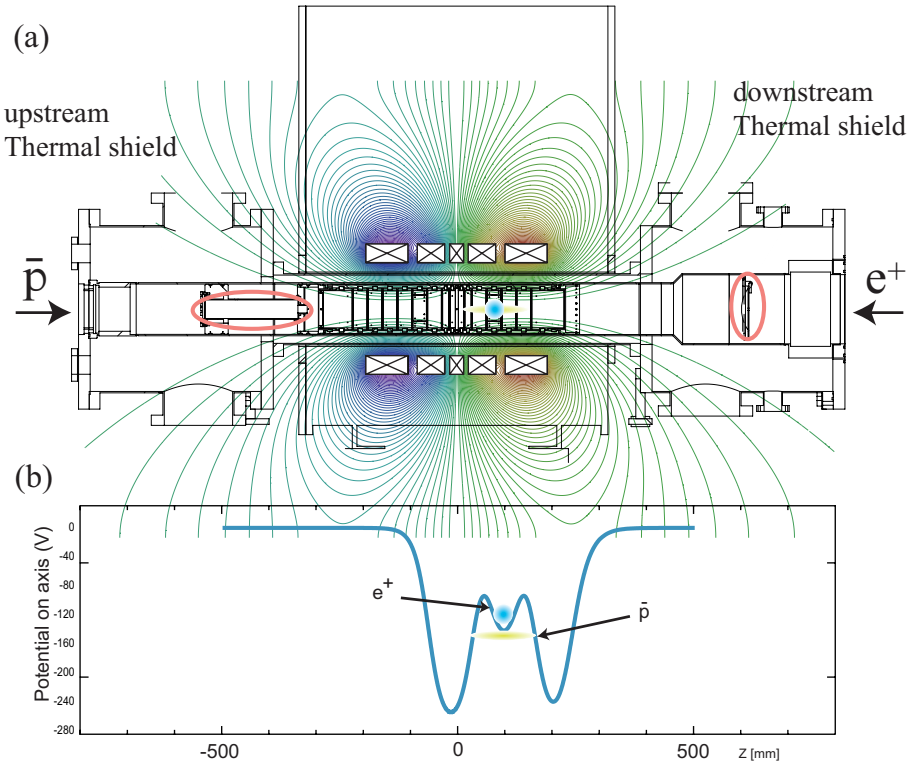

Figure 20: *(a): A cross section of the cusp trap with magnetic field lines. (b): A typical nested potential configuration along the axis.*

[48] configuration used in 2009 is shown by the light-blue line in fig. 20(b), which indicates that e^+s are localized 10cm downstream from the center of the Cusp-MRT, and $\bar{p}$s are localized 7 and 13cm downstream once they are fully cooled. The initial relative energy between $\bar{p}$s and e^+s was tuned by varying the depth of the e^+ trapping potential.

Pulsed $\bar{p}$ beams of 150 eV were injected from the MUSASHI accumulator and trapped in the downstream side of the Cusp-MRT passing through $B = 0$ region. A typical number of $\bar{p}$s trapped was 1–3 $\times 10^5$ when one AD shot was used.

As the first step, temporal annihilation patterns of $\bar{p}$s were studied for various mixing conditions of $\bar{p}$s and e^+s. Figures 21 (a) and (b) show such patterns when $\bar{p}$s were trapped in the nested trap configuration without and with e^-s, respectively. It is seen the annihilation rate increased when e^-s were in the nested trap, and cooled $\bar{p}$s, which is due primarily to higher annihilation rate of slower $\bar{p}$s with residual gas molecules. Figures 21 (c) and (d) show the case for 5 and 28 stacked positrons, respectively. The annihilation rate with 5 stacked positron pulses (fig. 21 (c)) is similar to that in fig. 21 (a) at the beginning ($t < 40s$) and then slowly increases, which levels off at ∼200s or so with the annihilation rate higher than that in fig 21 (a), i.e., $\bar{p}$s were cooled even with 5 stacked e^+s. In the case of 28 stacked e^+s, the annihilation rate increased drastically due to faster cooling of $\bar{p}$s. In both cases (figs 21 (c) and (d)), the e^+ cloud was contaminated with ions of a similar number as e^+s. To observe the effect of e^+s, a scheme to remove ions from the positron trap were invented. An example of the annihilation pattern without ions is shown in Fig 21 (e) for 60 stacked e^+s. Although the peak annihilation rate was lower than in the case of fig 21 (d), still the annihilation enhancement is clearly seen at t ∼30s[8]. We also made the mixing experiments with

[8]This decrease of the annihilation rate can be due to the trapped ions and/or the density change of e^+s during the ion removal procedure.

smaller energy difference (5 eV), which is shown in fig. 21(f) (it was 90 eV in the case of figs. 21(a)-(e)). Figure 21(f) shows that the annihilation rate is maximum at the beginning of mixing and then monotonically decreases, i.e., the peak appeared ∼30s earlier than the case of fig. 21(e). When $\bar{p}$s pass through the $B = 0$ region at the center of the cusp trap, a part of them acquire considerable amount of transverse momenta, and so are reflected before reaching the positron trapping region of the nested trap when the relative energy is small, which would be the reason of smaller annihilation rate and longer tail (see fig. 21(f)) as compared with fig. 21(e).

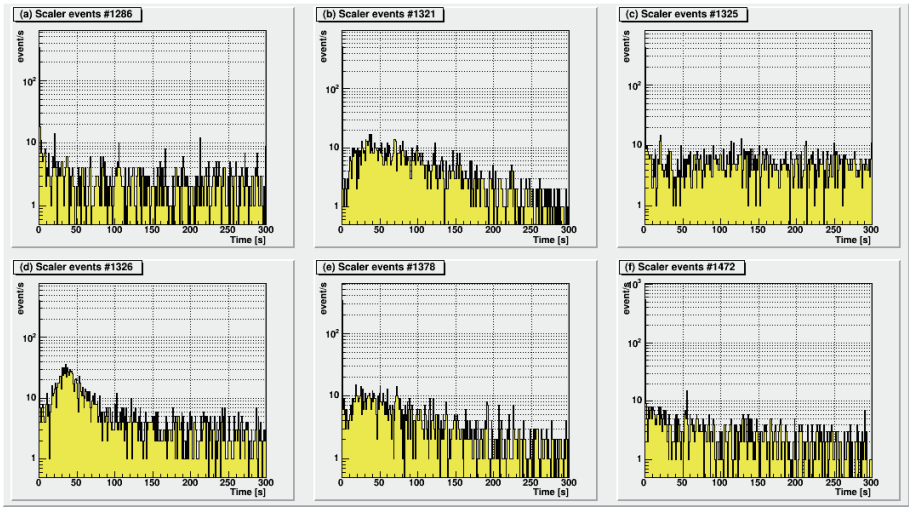

Figure 21: *$\bar{p}$ annihilation events during mixing (a) without any coolant (neither e^- nor e^+), (b) with e^-, (c) with 5 stacked e^+s and contaminant ions, (d) with 28 stacked e^+s and contaminant ions, (e) with e^+ but without contaminant ions, and (f) with e^+ without contaminant ions with smaller relative energy difference between $\bar{p}$s and e^+s (see the text for more details).*

3.3.3 Annihilation position distribution analyses

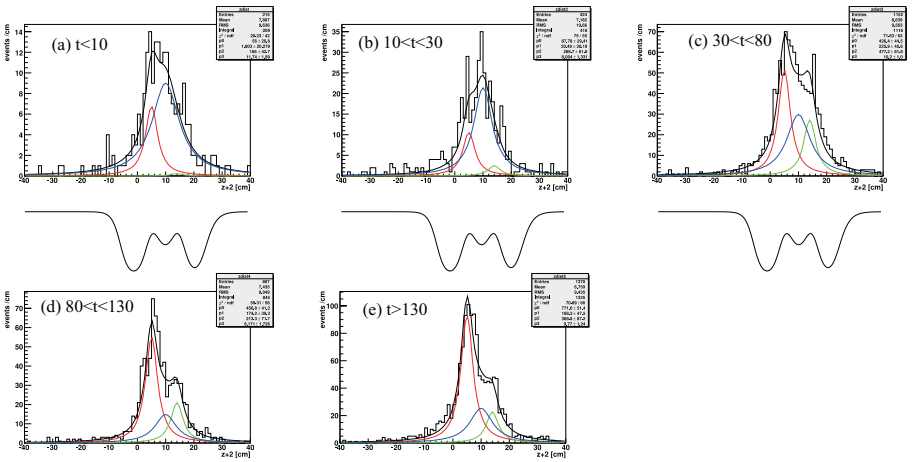

Figure 22: *Annihilation distribution of $\bar{p}$ along the z-axis for (a) $0\ s < t < 10\ s$, (b) $10\ s < t < 30\ s$, (c) $30\ s < t < 80\ s$, (d) $80\ s < t < 130\ s$, and (e) $t > 130\ s$.*

Figures 22 (a)-(e) show $\bar{p}$ annihilation distributions along the z-axis obtained by the 3D detector for different time ranges from the beginning of the mixing (see the caption of fig. 22 for more details). In the

case of figs. 22, ions in the positron trap were removed before experiment like in the case of fig. 21(e). The annihilation distribution was fitted by three Lorentzian curves having their centers near the extremum points of the nested potential (see fig. 22). The black solid curve and three solid curves (red, blue, and green) in each figure show the results of the fitting. The fitting reveals that (1)the annihilation component centered at the positron trap ($z \sim$ 10cm) dominates in the fist 30s or so, and then decreases gradually, (2)the component centered at $z \sim$ 6cm presents from the beginning and grow continuously, and (3)the component at $z \sim$14cm is very weak at the beginning and then grows although always smaller than the component at $z \sim$6cm. Naturally, the component centered at $z \sim$10cm is the candidate of $\bar{\mathrm{H}}$ formation although the probability of forming $\bar{p}p$ at the positron trapping region is also high. It is noted that the period when the component centered at $z \sim$10cm is strong coincides with the period when the annihilation rate is maximum in fig. 21(e). In other words, the first several tens seconds from the time of mixing is the key period for the $\bar{\mathrm{H}}$ synthesis.

3.3.4 RF heating

We also tried to observe the $\bar{p}$ annihilation pattern and the annihilation rate by heating up e^+ cloud by applying RF [49]. The curve shaded blue in fig. 23 shows $\bar{p}$ annihilation events with e^+ and ions without RF heating. The annihilation peak is seen $\sim$30s after the start of the mixing. The curve shaded yellow in fig. 23 shows a case when a RF was on with its frequency tuned near the axial oscillation frequency of trapped e^+ with 10 V_{pp} in the first 50 s. It is interesting to observe that the annihilation peak delayed by $\sim$50 s.

Further tests were also performed by periodically applying RF [49] with much lower RF power. In this case, no clear differences were observed.

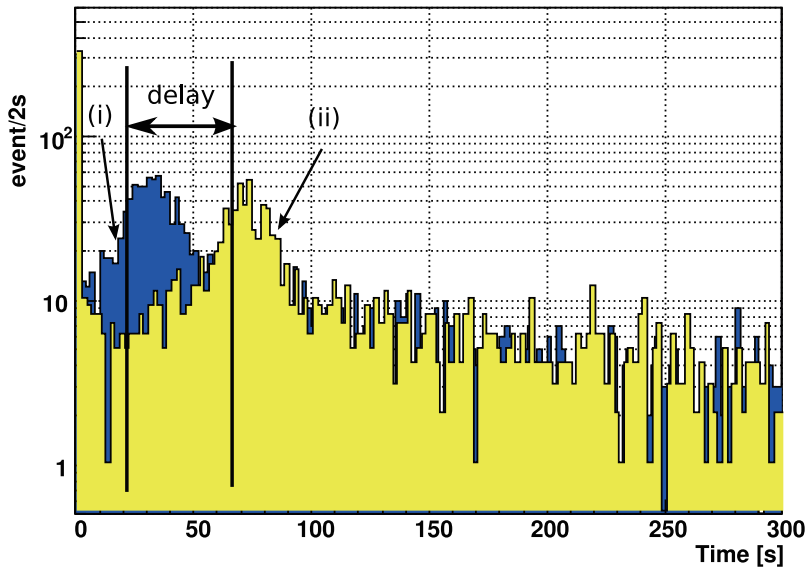

Figure 23: *Annihilation rates of $\bar{p}$s without (blue) and with (yellow) RF in the first 50 s when $\bar{p}$s were mixed with e^+s containing ions.*

3.3.5 Field ionization

Further, we tried to detect $\bar{\mathrm{H}}$ atoms in high Rydberg states via field ionization [47]. For this, a field ionization well was periodically turned on and off at the upstream spindle Cusp as shown in fig. 24 expecting that $\bar{p}$ annihilations are detected when the well was turned off. An example of the annihilation pattern is given in fig. 25(a), which shows high annihilation rate whenever the field-ionization trap was opened. Unfortunately and surprisingly, even higher annihilation counts were observed when no e^+s were in the nested trap as

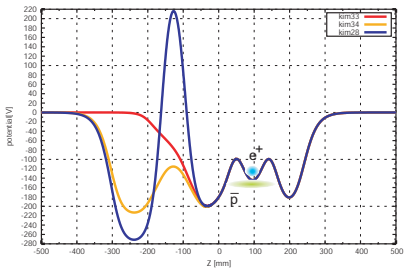

Figure 24: *Sequential potential changes for dumping $\bar{p}$s in the upstream field-ionization trap (blue → orange → red).*

shown in fig. 25(b). It is noted that the potential variation near the $\bar{p}$ trapping region was as small as a few V, and the potential barrier was several tens eV higher than the energy of trapped $\bar{p}$s, i.e., the chance for these $\bar{p}$s to leak out the trapping region should be extremely small. To overcome this difficulty, better potential settings and on and off procedures were sought, and eventually some reasonable configurations were found. Experiments with relatively small number of e^+s (10 stacks) were made with this configuration, but no positive results were observed. Unfortunately, this experiment was done in the last moment of the extended beamtime, and further study was postponed to 2010.

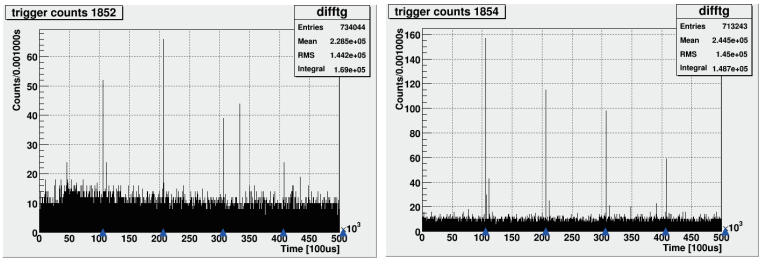

Figure 25: *Counts of 3D detector triggers when (a)$\bar{p}$s are mixed with e^+s, and (b) only $\bar{p}$s were trapped.*

3.4 3D detector for the cusp trap

3.4.1 Detector description

The vertex detector consists of four different modules of scintillator rods aimed at detecting charged pions produced by $\bar{p}$ annihilations. Each module is assembled by coupling two layers of 64 rods of plastic scintillators (Polystyrene Dow Styron 663 W + 1% PPO + 0.03% POPOP, white capstocking TiO_2). Each rod is 15 x 19 x 960 mm^3 with a central hole of diameter 2 mm, where is placed a WLS Kuraray Y-11 green fiber 1 mm in diameter; the gap between the green fiber and the hole is filled with optical glue, which enables a particle detection efficiency $> 90\%$ on the full extent of the rod. So, the sensitive area of each module is 960^2 mm^2. The rods of the two layers are crossed by 90° to measure the coordinate of the pion intersection point along two perpendicular directions. Two modules are placed on each side of the cusp trap, with respect to the antiproton beam from MUSASHI.

The fibers emerge from the rods on both sides, and both ends are connected to the outside of the container and could be read out in principle, even though only one end is currently utilized. The signal coming form each fiber is read through a mechanical-optical connection with Hamamatsu H7546B 64-channel photomultipliers (PMT), whose slots are only partially filled (every second slot is connected to the fiber) to avoid cross-talk problems. So, every PMT is reading precisely half a layer.

By the way, the unused terminations of the green fibers of the horizontal rods of the external modules, bundled together for a semi-layer, are connected to a P30CW05 photomultiplier by Electron Tubes to produce the trigger signal. Namely, the trigger signal for the data acquisition system is taken by the coincidence of the signal coming form the two mentioned layers. The background counting rate ($\sim$ 1 Hz) was low enough to ensure a negligible level of spurious events.

3.4.2 Readout electronics

In 2009 the electronics has been renewed because of an electromagnetic noise problem found in 2008 that prevented the detector from working properly. In particular, a new set of frontend boards (FEBs) has been designed and produced. The acquisition chain of the 3D detector consists in these new FEBs (see below for a short description of their characteristics and their differences from the previous version) connected to the VME readout system. Each new FEB is connected to a PMT by a dedicated socket: this is a crucial difference between the new FEBs and the old ones where the system with the flat cables (lengths from 30 to 50 cm) turned out to work as antennas. One VA64TAP2.1 ASIC (Gamma Medica, Ideas - Norway, same as 2008) provides the analog signal shaping and discrimination, then the signals are digitized by means of a 12-bit ADC hosted on the FEB itself. This is another new feature with respect to 2008 when the ADCs were VME modules (CAEN V550).

In order to improve the maximal rate supported by the data acquisition, a zero-suppression data acquisition mode has been implemented, consisting in recording only the ADC signals above a threshold proportional to the noise-rms level. This should make it possible to bear a trigger rate of about 1000 Hz without significant data losses.

3.4.3 Positioning

After the experience we gained from our 2008 run, that pointed out the importance to have a precise positioning of the modules in order to improve the accuracy of the vertex reconstruction to the level predicted by the Monte Carlo simulation, each module was equipped with a drilled brick, used as reference position, in which it was possible to fit the basement of a mirror whose coordinates could be measured within less than 1 mm by the CERN geometers with a purposed theodolite. We have benefited of two geometers' surveys, the first on September 1st [50], the second (needed after the reinstallation of the cusp trap apparatus in the extended beamtime) on November 30 [51].

3.4.4 Monte Carlo simulation

Simulations of the apparatus based on Geant 3 have been used to design the detector geometry and to test and subsequently improve the reconstruction program, which is based on a combinatorial algorithm similar to the one already used for the tracking detector in the $\bar{p}$-nucleus annihilation cross-section measurement. This assumes straight tracks (passing for the rods carrying a signal above a fixed threshold) and as has proved to be effective in a wide region of the cusp trap, where most of the annihilations are expected. Some results of the reconstruction software applied to the simulated annihilation are reported in table 3.

The simulation was performed by generating the antiproton annihilations in x=y=z=0 (here and in the following, z is the coordinate along the beamline and the cusp trap axis, y is the vertical coordinate, and x is the horizontal coordinate perpendicular to z; the origin of such a coordinate system is chosen to be close to the center of the cusp trap). The spatial resolution of the reconstructed vertices is mainly limited by the multiple scattering inside the material (especially in the cusp trap apparatus, rather than in the modules themselves) and by the strong, highly non-uniform, magnetic field of the cusp trap.

σ_z	1.8 cm
σ_y	2.1 cm
σ_x	8.4 cm
trigger efficiency	4.2% of the annihilations
reconstruction efficiency	41% of the triggers

Table 3: *Monte Carlo results*

3.4.5 Experimental results

The detector was installed twice: the first time on August 21, and again in the extended beamtime, on November 25. After the first installation, a list of tests were performed to check the detector performance. Unfortunately, because of the lack of time, these tests have not been repeated during the extended beamtime.

Here, we report about a "detector position calibration" performed by trapping the antiprotons in different z-regions by suitably setting the electrodes voltages (see Fig.26a) and cooling the antiprotons with electrons. As a consequence, the reconstructed vertices accordingly changed their location (see Fig.26b).

If we plot the mean value of the Gaussian interpolating function of the reconstructed vertices z-distribution as a function of the expected mean annihilation position (i.e. the z-position of the maximum of the electrostatic potential profile, see Fig.26a) we get the results shown in Fig.26c, where we can appreciate a very linear behavior with an angular coefficient equal to 1.06 ± 0.02 (close to 1 as expected) and an offset equal to 0.3 cm $\pm$ 0.2 cm (close to 0 as expected).

3.4.6 Future plans

The shutdown time will be essential to improve the 3D detector performance. In particular, we plan:

- to investigate the reason why sometimes we observed a malfunctioning of a couple of front-end boards, leading to an amplification by an order of magnitude of the noise for a limited time duration (some seconds) but sufficient to reduce substantially the reconstruction efficiency;
- to equalize the efficiency of the different multichannel photomultipliers by supplying a different voltage to each of them;
- to set up a checking system by means of LEDs placed at the free end of the fibers.

3.5 Antihydrogen sextupole beamline

The ASACUSA collaboration is planning to measure the ground-state hyperfine splitting (GS-HFS) of antihydrogen ($\overline{\mathrm{H}}$) using an atomic beam apparatus similar [52, 53] to the ones which were used in the early days of hydrogen HFS spectroscopy. The apparatus will use antihydrogen atoms produced either in a superconducting radiofrequency Paul trap or in a superconducting cusp trap (i.e. anti-Helmholtz coils). In the former case, the apparatus would consist of two sextupole magnets for the selection and analysis of the spin of the $\overline{\mathrm{H}}$ atoms, respectively, and a 1.4-GHz radiofrequency resonator in between them to flip the spin. In the latter case, the first sextupole could be omitted because the cusp trap should be able to provide a partially polarized antihydrogen beam. This atomic beam method has the advantage that antihydrogen atoms of temperatures up to 150 K can be used.

During 2009, the work towards building the radiofrequency resonator started at CERN with the help of the BE-RF group. Previous simulations [54] showed that with a double stripline design the required strength and homogeneity of the oscillating magnetic field can be reached. Major vacuum components

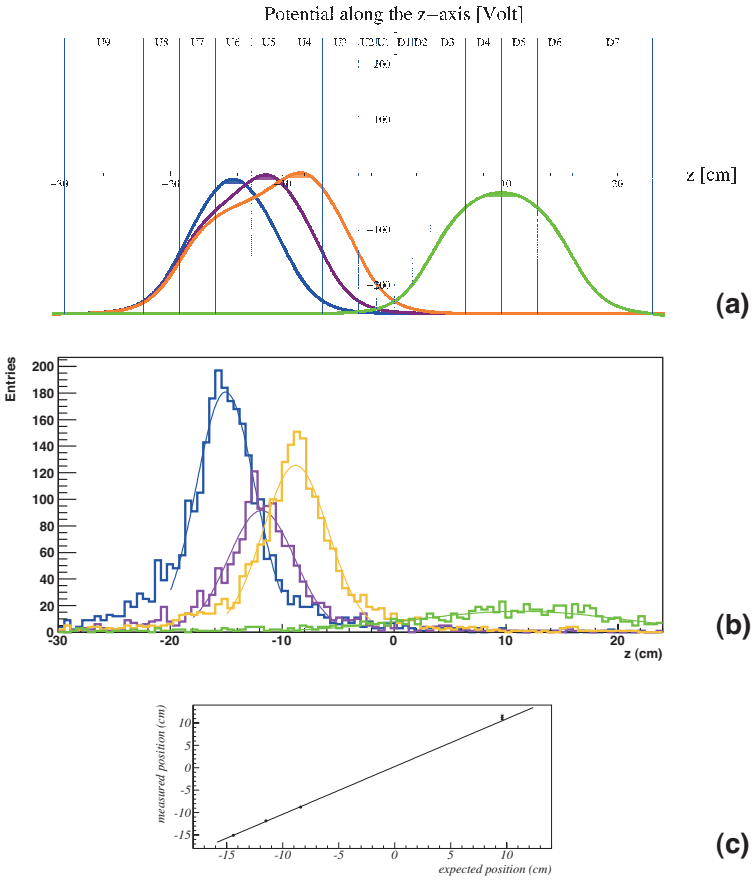

Figure 26: *(a): electrostatic potential along the trap axis for different trapping configurations (the shaded area indicates where antiprotons should be trapped once cooled); (b) z-distribution for the reconstructed vertices; (c) plot of the centre of the measured distribution in (b) versus the expected position deduced from (a).*

(pumps, gauges, gate valves) have been purchased, and the detailed engineering design of the resonator will continue in 2010, together with the design of the magnetic shield around the resonator. This shielding is necessary because of the strong stray magnetic fields of the cusp trap and the sextupole magnet.

Another important component of the atomic beam apparatus is the superconducting sextupole magnet. This device has been ordered in 2009 through CERN from Tesla Engineering in the UK, following a market survey and a tendering process at CERN. Tesla will design and build the magnet based on our detailed specifications. The deadline for the delivery of the magnet is the end of February, 2010. After the magnet has arrived to CERN, it will be tested and commissioned, so that it is ready for the beam time in 2010. During the second half of the cusp trap beam time period the magnet will be connected to the cusp trap exit (i.e. without the RF resonator between the two) to test the performance of the combined vacuum systems and the effect of the sextupole magnet on the particles emitted from the cusp trap, which will hopefully include antihydrogen atoms too. To detect these particles, 10-cm diameter multi-channel plate (MCP) detector will be installed downstream of the sextupole magnet.

3.6 Summary of 2009 and plan for 2010

We had important progress and encouraging results in 2009 such as (1) more than ten times higher accumulation rate of positrons than the last year, (2) positron compression in the non-uniform cusp magnetic field, (3) stable mixing of antiprotons and positrons followed by cooling of antiprotons in the non-uniform cusp

magnetic field, (4) higher antiproton annihilation rate for larger number of positrons, (5) delayed annihilation with RF field, (6) proper potential configuration for field-ionization trap, (7)non-destructive monitoring of the number of antiprotons, etc. However, the confirmation of $\bar{\mathrm{H}}$ atom formation was postponed to the beamtime in 2010.

The temperature of the e^+ plasma is the crucial parameter particularly for the field-ionization experiments. We have already found several noise sources, and succeeded to reduce them. Further noise reduction will be continued during the winter shutdown. A cryogenic electronic filter will be installed to achieve ideal 4 K environment with a low noise level in the Cusp-MRT. Two new NEG (non-evaporable getter) pumps (1300 l/s each) are going to be installed to improve the vacuum for longer $\bar{p}$ lifetime. At the same time, thermal contacts between the Cusp-MRT and the cold bore will be improved to get better vacuum and lower temperature positrons.

3.6.1 Positron transfer section in 2010

As soon as the formation of $\bar{\mathrm{H}}$ atoms is confirmed, the experimental setup will be rearranged as shown in fig. 27(a) moving the pre-positron accumulator upstream of the cusp trap, and also installing the superconducting sextupole magnet in the downstream, which enable at least to extract $\bar{\mathrm{H}}$ beams downstream of the cusp trap, the next step to the goal, the spectroscopy of ground-state hyperfine structure of $\bar{\mathrm{H}}$ atoms.

To realize this, a new beam line for the low energy positrons is designed and under construction, which consists of four solenoids as shown in fig. 27(a). Since the energy of the positrons is less than 200 eV, a magnetic guide field is more efficient than quadrupole magnets and dipole magnets.

The color contour plot shown in fig.27 (b) is an example of magnetic field distribution optimized for the 100-eV e^+ transport. The positron pre-accumulator and the MUSASHI $\bar{p}$ accumulator are put at the upper and lower left, respectively, and the cusp trap is set at the lower right. Typical field strength of the transfer section is $\sim$ 800 G. One of the solenoid coils right after the positron source will be water cooled, so that it can provide magnetic field continuously if necessary.

Simulated trajectories of 100 eV positrons from the positron pre-accumulator to the cusp trap are also shown in fig.27 (a). Assuming that the perpendicular energy of positrons are less than 1 eV, the initial position of positrons are set in a 6mm$\times$6mm square centered on the z-axis. It is seen that most of positrons are transferred successfully.

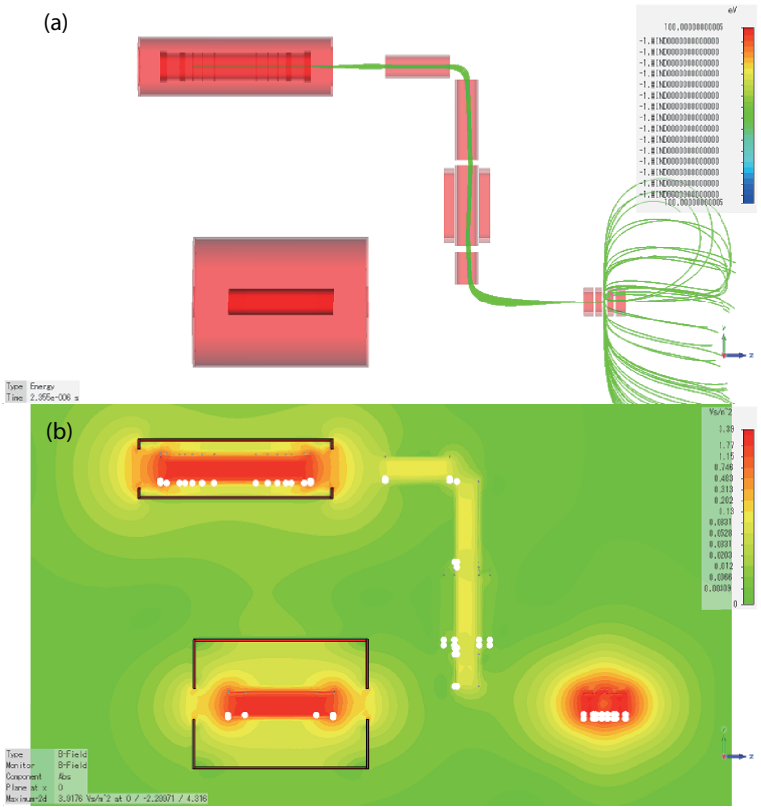

Figure 27: *(a) A new configuration of the positron pre-accumulator (top-left), the MUSASHI accumulator (bottom-left), and the cusp trap (right) with trajectories of 100eV e^+s extracted from the positron pre-accumulator. (b) Contour plot of the B field. Magnetic shields of MUSASHI and positron trap are included. Typical field strength of the transfer section is* $\sim$ *800 G.*

4 Ionization of atoms and molecules by slow antiprotons

Our run in 2009 was hampered by two problems: During the first week, we had problems getting a proper beam quality to the AIA apparatus as discussed in Section 3.1. This was solved when it was realized that we needed more AD shots accumulated in the MUSASHI trap to get the rotating wall compression to work than we had used the previous years. Then, ready to take data, we had almost no useable beam from the AD during the following week of August 10-16.

We did, however, measure a few data points for the ionization of molecular hydrogen, which have turned out to be important: At 10 keV, the new data confirm the magnitude of our measurements obtained at LEAR, where a very different experimental method was employed, see figure 28.

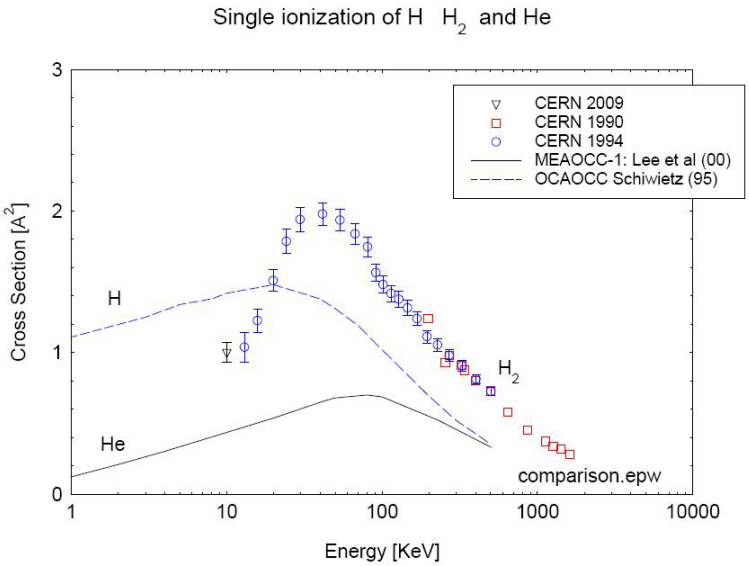

Figure 28: *The cross sections for single ionization of helium, atomic hydrogen and molecular hydrogen for antiproton impact. The H_2 data are from refs [55] and [56] and from the 2009 run (triangle). The dashed curve [57] and the full drawn curve [58] are theoretical calculations, which agree with our helium data [59] as well as our H data [60].*

From Figure 28 it can be seen, that the energy dependence of the ionization cross section for the two atomic targets is quite different than that for the molecular target, in that the molecular cross section decreases much faster with decreasing energy than do the atomic cross sections. This is at first sight puzzling, since H_2 has many properties common with H and He. It consists of two H atoms, and it has two positive charges surrounded by two electrons, such as is the case for He. We believe that the drastic decrease of the cross section with decreasing impact energy is due to the molecular structure of H_2: As a slow antiproton approaches an atom, its nuclear charge is screened by up to one unit charge, and it is very likely that one atomic electron is released. However, if a slow antiproton approaches a molecule, even if one of the nuclear charges are completely screened by one charge unit, there is still one or more nuclei around, which can temporarily bind all the molecular electrons, see Figure 29.

In our next run, we plan to measure the H2 cross section to lower impact energies, as well as the ionization cross section for atomic hydrogen, which is measured only down to 30 keV.

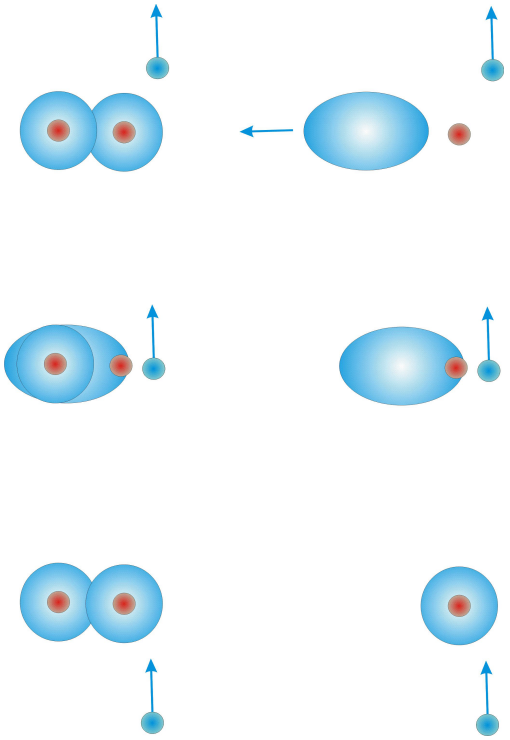

Figure 29: *The approach of a slow antiproton to a molecular (left) and to an atomic target (right).*

5 Antiproton-nuclei cross sections experiment at 100 keV

5.1 2009 Measurements

In 2009 the second phase of the measurement of the antiproton annihilation cross section (σ_{ann}) has been started. In the first phase the measurement was done at 5.3 MeV on 4 targets (Mylar, Ni, Sn, Pt) and the resulting annihilation cross section has shown a dependence on the mass number A which follows the $A^{2/3}$ rule (the results have been submitted to Nuclear Physics A). In the new phase the measurement has been extended down to 100 keV where no data exist. In fact the existing data at the lowest energies were achieved in the LEAR era at 0.5-1 MeV of the antiproton kinetic energy. They concern only light nuclei and show that σ_{ann} does not increase with A as expected (”saturation effect”).

The main difficulty in performing a measurement of σ_{ann} at AD is due to the fast pulsed extraction of the antiproton beam and to overcome this limitation we have exploited the experience gained with the 5 MeV measurement performed in 2008.

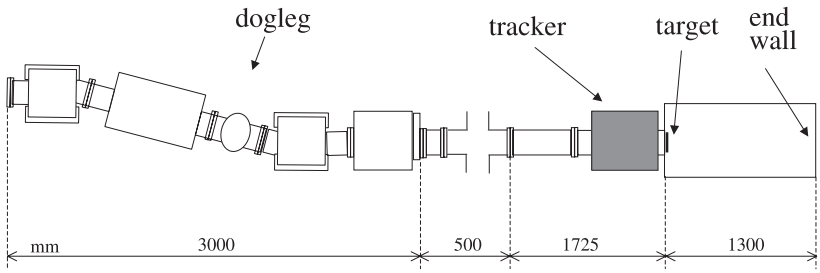

Figure 30: *Sketch of the ASACUSA apparatus for σ_{ann} measurement of $\bar{p}$ at 100 keV.*

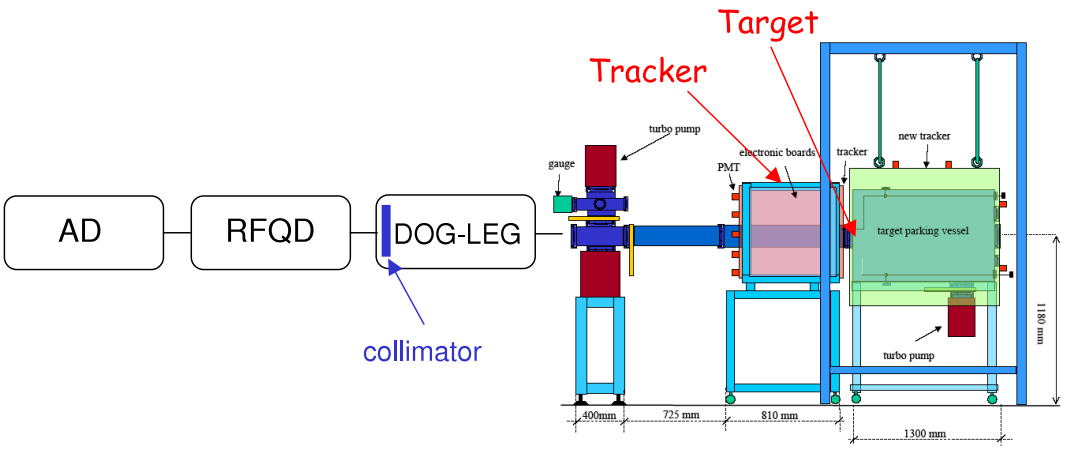

Figure 31: *ASACUSA experimental set-up for σ_{ann} measurement of $\bar{p}$ at 100 keV.*

The apparatus for 100 keV is the same as used for the 5 MeV measurement with the addition of the RFQD and the dog-leg, see Fig. 30 and Fig. 31. As in the 5 MeV measurement, the so called "multiple extraction" option has been used: the 100-MeV/c antiprotons circulating in the AD are first bunched into six buckets (each containing approximately 5×10^5 antiprotons) and then sequentially extracted to the experiment using a kicker magnet installed in the AD. The selected time duration of each pulse reaching the experiment was around 40–50 ns.

The 5.3 MeV antiproton beam from the AD is decelerated down to 100 keV by the ASACUSA RFQD. Then it passes through a small hole (2 mm in diameter) of an iris positioned at the entrance of the dog-leg momentum selector. The purpose of the iris is to reduce the radial halo of the antiproton beam in order to prevent annihilations along the beam line just in front of the target which can blind the detector if they are numerous.

Since the σ_{ann} value is proportional to the ratio of the annihilation events in the target and the antiproton flux crossing the target, the apparatus has been designed in order to count the events in the target by means of the tracker detector (which is able to reconstruct the tracks of the charged pions emitted after the antiproton annihilation) while the beam is monitored by a scintillator read by a hybrid photodetector (HPD) device.

The targets are made by carbon foils (8 cm in diameter) with sputtered metals. The available thicknesses (70 nm for carbon and 21, 32, 13 nm for Ni, Sn and Pt respectively) have been chosen in order to have few annihilations on the targets per pulse assuming that the σ_{ann} scales as $A^{2/3}$ (it must be pointed out that the present availability of carbon supports with very small thicknesses could be very useful also for the measurement at higher energies thanks to the negligible contribution given to the total number of annihilation events). The energy degradation of the 100 keV antiprotons is expected to be limited to few tens of keV. The expected background comes from the antiproton annihilations occurring not on the target.

In 2009 the assigned beam time was devoted to verify the actual feasibility of the 100 keV measurement and particularly to check the effect of the background on the measurement.

In Fig. 32, below the sketch of the experimental set-up, the signals seen by the detectors are plotted for one antiprotons pulse. The upper distribution is the time distribution seen by the large scintillator plane (about 0.9 m^2, placed parallel to the antiproton beam and longitudinally behind the target) while the lower one is the time distribution measured by one layer of the cylindrical tracker (placed around the antiproton beam line just before the target), see Fig. 31. In the upper distribution we can clearly distinguish the signals coming from the regions corresponding to the iris, the target and the end wall of the target vessel. The signal from the target region results to be well separated in time from the others signals as a consequence of the spatial distances between the different regions, the low velocity (4.4 mm/ns) of the antiprotons and the limited time duration of the antiproton pulses (40–50 ns). This result is even clearer in the lower distribution

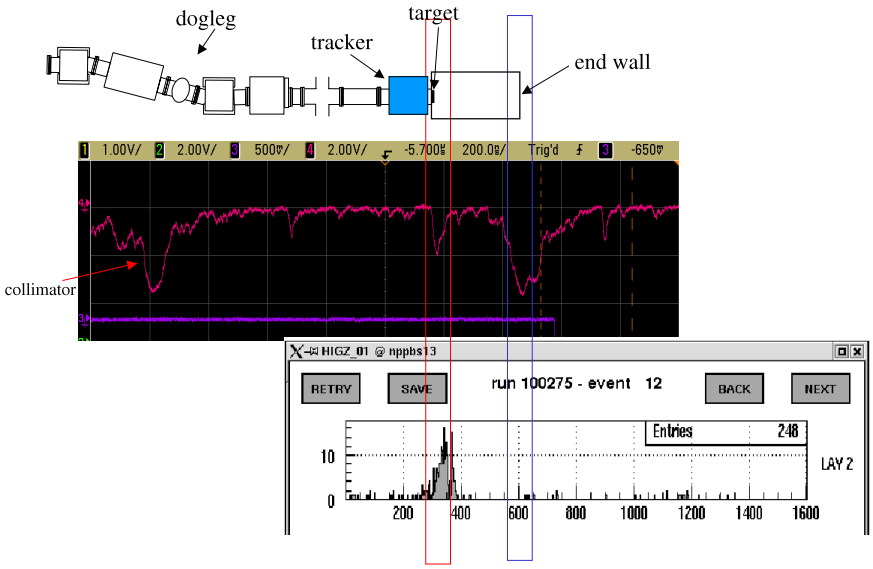

Figure 32: *Signals seen by the detectors for one antiprotons pulse in correspondence with the apparatus layout.*

where actually just the annihilations from the target region appears since the detection of the other signals is disadvantaged by the geometrical position of the tracker.

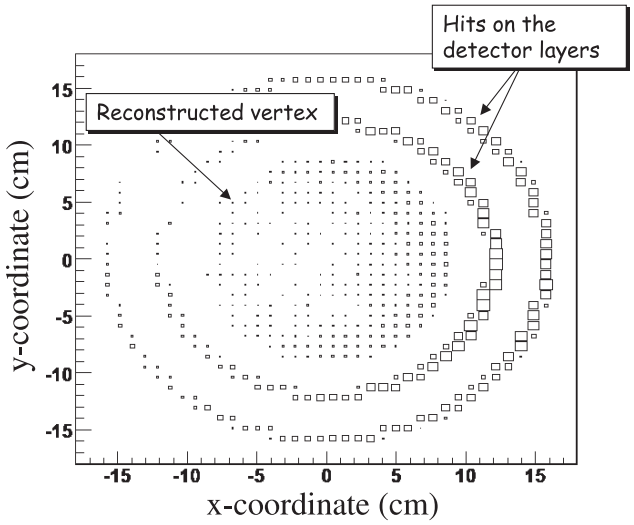

Figure 33: *y- versus x-coordinate of the reconstructed vertices.*

It must be pointed out that the signal from the target region is mostly due to antiproton annihilation on the thick ring (inner radius equal to 4 cm) supporting the target and only a very small percentage is due to annihilation on the real target (radius less than 4 cm) as confirmed by the scatter plot in Fig. 33 of the transverse coordinates of the reconstructed events. From this plot it is evident that the parameters of the dog-leg device are not set at the best for the present data since the antiproton beam need to be better centered and better focused.

The present data indicate that the main sources of background are under control and with an increase of the quality of the antiproton beam on the target the 100 keV measurement is feasible.

5.2 Plans for 2010

In 2010 we plan to continue the experiment of antiproton-nucleus collision at 100 keV. The aim is to measure the annihilation cross sections for different nuclei with our thin targets (C, Ni, Sn, Pt). As we have seen from our 2008 data-taking, the success of the measurement will depend on the quality of the antiproton beam arriving at the target after the RFQD deceleration and the dog-leg spectrometer. We are improving this quality by means of a dedicated study of the best setting parameters of the dog-leg in order to address the beam on the target reducing the annihilations on the surrounding thick frame which support the target itself. We will use a quite sophisticated multi-particle tracking simulations program which accounts for non-linear effects such as chromatic aberration and is adequate to study the beam halo.

We will also substitute the used iris having a fixed value of the hole diameter with one with variable diameter and we will employ a removable small detector to be put at the target position for monitoring the beam.

In addition a quasi-total cancellation of the electron background, due to π–μ–e decay with a lifetime of 2.2 μs, will be done by building a wall of concrete to screen the tracker. Monte Carlo simulations with Geant4 package indicates that a thickness of 1.5 m is enough for our purpose.

6 Development of a superconducting radiofrequency Paul trap for antiprotons

In 2009 the ASACUSA collaboration, together with support from the CERN AB division, ECR group, CERN cryogenic laboratory, central workshop, and brazing workshop, continued assembly of the radiofrequency Paul trap to confine antiprotons. The main RF cavity vessel made of oxygen-free high conductivity copper was completed, and sputtered with niobium. The quadrupole electrodes made of pure niobium which will be used to trap the antiprotons were constructed, and RF tests will be carried out in early 2010. The cryogenic systems were leak-tested and will be tested following the completion of a pumping line now being installed in the CERN ECR cryolab.

We constructed a series of five segmented scintillation detectors which will be placed outside the Paul trap to measure the pions emerging from the antiproton annihilations. Our design is similar to the one used by the T2K neutrino experiment. Green wavelength-shifting fibers were embedded in either extruded or machined grooves in the scintillator. The collected light will be read out using 300 multipixel silicon photomultipliers of diameter $\sim$ 1 mm. A readout board using analog ASIC and field programmable gate arrays (FPGA)s are now being constructed. We intend to test the system in 2010 at the test beamline in CERN PS.

References

[1] M. Hori and A. Dax, *Opt. Lett.* **34**(8), 1273 (2009).

[2] M. Hori *et al.*, *Phys. Rev. Lett.* **96**, 243401 (2006).

[3] V. I. Korobov, *Phys. Rev. A* **77**, 042506 (2008).

[4] M. Hori and V. Korobov, submitted to Phys. Rev. A.

[5] P. J. Mohr, B. N. Taylor, D. B. Newell, *Rev. Mod. Phys.* **80**, 633 (2008).

[6] T. Yamazaki, N. Morita, R. S. Hayano, E. Widmann, J. Eades, *Physics Reports* **366**, 183 (2002).

[7] R. S. Hayano, M. Hori, D. Horvath, E. Widmann, *Reports on Progress in Physics* **70**, 1995 (2007).

[8] M. Hori, K. Yamashita, R. S. Hayano, T. Yamazaki, *Nucl. Instr. Meth. Phys. Res. A* **496**, 102 (2003).

[9] M. Hori *et al.*, *Phys. Rev. Lett.* **87**, 093401 (2001).

[10] G. Gabrielse *et al.*, *Phys. Rev. Lett.* **82**, 3198 (1999).

[11] C. Amsler et al., *Physics Letters B* **667**(1-5), 1 (2008), Review of Particle Physics.

[12] R. Holzwarth *et al.*, *PRL* **85**(11), 2264 (2000).

[13] T. Udem, R. Holzwarth, T. W. Hänsch, *Nature* **416**, 233 (2002).

[14] H. Yamaguchi *et al.*, *Phys. Rev. A* **70**, 012501 (2004).

[15] M. Iwasaki *et al.*, *Phys. Rev. Lett.* **67**, 1246 (1991).

[16] T. Yamazaki *et al.*, *Nature* **361**, 238 (1993).

[17] T. Yamazaki, N. Morita, R. S. Hayano, E. Widmann, J. Eades, *Phys. Rep.* **366**, 183 (2002).

[18] R. Hayano, M. Hori, D. Horváth, E. Widmann, *Reports on Progress in Physics* **70**(12), 1995 (2007).

[19] D. Bakalov and V. I. Korobov, *Phys. Rev. A* **57**, 1662 (1998).

[20] V. I. Korobov and D. Bakalov, *J. Phys. B* **34**, L519 (2001).

[21] E. Widmann *et al.*, *Phys. Rev. Lett.* **89**, 243402 (2002).

[22] T. Pask *et al.*, *J. Phys. B: At. Mol. Opt. Phys* **41**, 081008 (2008).

[23] T. Pask *et al.*, *Physics Letters B* **678**, 55 (2009).

[24] V. I. Korobov and Z.-X. Zhong, *Physical Review A* **80**, 042506 (2009).

[25] A. Kreissl *et al.*, *Z. Phys. C* **37**, 557 (1988).

[26] E. Hu *et al.*, *Nucl. Phys. A* **254**, 403 (1975).

[27] B. L. Roberts *et al.*, *Phys. Rev. D* **12**, 1232 (1975).

[28] T. Pask, *Hyperfine Interactions* **194**, 7 (2009).

[29] D. Bakalov and E. Widmann, *Physical Review A* **76**(1), 12512 (2007).

[30] V. Korobov, *Physical Review A* **73**(2), 22509 (2006).

[31] J. Sakaguchi *et al.*, *Nucl. Instrum. Methods Phys. Res. A* **533**, 598 (2004).

[32] M. Hori *et al.*, *Physical Review Letters* **96**(24), 243401 (2006).

[33] A. Mohri and Y. Yamazaki, *Europhys. Lett.* **63**, 207 (2003).

[34] N. Kuroda *et al.*, *Phys. Rev. Lett.* **94**, 023401 (2005).

[35] N. Kuroda *et al.*, *Phys. Rev. Lett.* **100**, 203402 (2008).

[36] D. J. Wineland and H. G. Dehmelt, *J. Appl. Phys.* **46**, 919 (1975).

[37] X. Feng, M. Charlton, M. Holtzscheiter, et al., *J. Appl. Phys.* **79**, 8 (1996).

[38] H. Higaki, N. Kuroda, K. Y. Franzen, et al., *Phys. Rev. E* **70**, 026501 (2004).

[39] C. M. Surko and R. G. Greaves, *Phys. Plasmas* **11**, 2333 (2004).

[40] H. Okamoto and H. Tanaka, *Nucl. Instr. Meth. A* **437**, 178 (1999).

[41] R. C. Davidson, *Physics of Nonneutral Plasmas, Chap. 10.* (Addison-Wesley, Redwood City, CA, 1990).

[42] T. J. Murphy and C. M. Surko, *Phys. Rev. A* **46**, 5696 (1992).

[43] P. J. Schultz and K. G. Lynn, *Rev. Mod. Phys.* **60**, 701 (1988).

[44] H. Saitoh, A. Mohri, Y. Enomoto, Y. Kanai, Y. Yamazaki, *Phys. Rev. A* **77**, 051403 (2008).

[45] M. Shibata, A. Mohri, Y. Kanai, Y. Enomoto, Y. Yamazaki, *Rev. Sci. Instrum.* **79**, 015112 (2008).

[46] M. Amoretti *et al.*, *Nature* **419**, 456 (2002).

[47] G. Gabrielse *et al.*, *Phys. Rev. Lett.* **89**, 213401 (2002).

[48] G. Gabrielse, S. L. Rolston, L. Haarsma, W. Kells, *Phys. Lett. A* **129**, 38 (1988).

[49] M. C. Fujiwara *et al.*, *Phys. Rev. Lett.* **101**, 053401 (2008).

[50] EDMS document #1019746 (https://edms.cern.ch/document/1019746).

[51] EDMS document #1053858 (https://edms.cern.ch/document/1034801).

[52] ASACUSA collaboration, Proposal CERN-SPSC-2005-002, SPSCP-307 Add.1 CERN, Geneva, Switzerland (2005).

[53] B. Juhász and E. Widmann, *Hyp. Int.* **193**, 305 (2009).

[54] T. Kroyer, CERN-AB-Note-2008-016.

[55] L. Andersen et al., *J. Phys. B* **23**, L395 (1990).

[56] P. Hvelplund et al., *J. Phys. B* **27**, 925 (1994).

[57] G. Schiewietz et al., Private communication (1995).

[58] T. G. Lee et al., *Phys. Rev. A* **61**, 062713 (2000).

[59] H. Knudsen et al., *Phys. Rev. Letters* **101**, 043201 and references therein (2008).

[60] H. Knudsen et al., *Phys. Rev. Letters* **74**, 4627 (1995).